FINAL TECHNICAL REPORT

GRANT: N00014-08-1-0973
PERIOD OF PERFORMANCE: July 2008-March 2009

"Proof-of-Concept Studies in Novel Guided Wave Methods for Metallic Structural Condition"

Michael Todd and Francesco Lanza di Scalea

Technical Point of Contact:

Michael Todd (PI)
Department of Structural Engineering
University of California San Diego
9500 Gilman Drive 0085
La Jolla, CA 92093-0085
Phone: (858) 534-5951
Fax: (858) 534-6373
Email: mdt@ucsd.edu

Business Point of Contact:

Michael Brown
Office of Contracts and Grants Administration
University of California San Diego
9500 Gilman Drive 0934
La Jolla, CA 92093-0934
Phone: (858) 534-2972
Fax: (858) 534-0280
Email: m2brown@ucsd.edu

UCSD Jacobs | Structural Engineering

COPIES:

1. ONR Program Manager, Dr. Paul Hess (Office of Naval Research, 875 N Randolph St, Arlington, VA 22203-1995)
2. ONRRO (ONR REG SAN-N66018, 140 Sylvester Rd, Bldg 140, Room 218, San Diego, CA 92106-3521)
3. DTIC (Defense Technical Information Center, 8725 John J Kingman Road, Ste 0944, Fort Belvoir, VA 22060-6218)
4. NRL (Naval Research Laboratory, Code 5596, 4555 Overlook Ave SW, Washington, DC 20375-5320)
5. Dr. Liming Salvino, NSWCCD, liming.salvino@navy.mil

REPORT DOCUMENTATION PAGE

Form Approved
OMB No. 0704-0188

1. REPORT DATE *(DD-MM-YYYY)*	2. REPORT TYPE	3. DATES COVERED *(From - To)*
15-06-2009	Final Technical Report	July 2008 - March 2009

4. TITLE AND SUBTITLE
Proof-of-Concept Studies in Novel Guided Wave Methods for Metallic Structural Condition

5a. CONTRACT NUMBER

5b. GRANT NUMBER
N00014-08-1-0973

5c. PROGRAM ELEMENT NUMBER

6. AUTHOR(S)
Todd, Michael
Lanza di Scalea, Francesco

5d. PROJECT NUMBER

5e. TASK NUMBER

5f. WORK UNIT NUMBER

7. PERFORMING ORGANIZATION NAME(S) AND ADDRESS(ES)
The Regents of the University of California; University of California, San Diego
9500 Gilman Drive, Mail Code 0934
La Jolla, CA 92093-0934

8. PERFORMING ORGANIZATION REPORT NUMBER

9. SPONSORING/MONITORING AGENCY NAME(S) AND ADDRESS(ES)
Office of Naval Research
875 North Randolph Street
Arlington, VA 22203-1995

10. SPONSOR/MONITOR'S ACRONYM(S)
ONR

11. SPONSOR/MONITOR'S REPORT NUMBER(S)

12. DISTRIBUTION/AVAILABILITY STATEMENT
B. Approved for public release; distribution unlimited.

13. SUPPLEMENTARY NOTES

14. ABSTRACT

Active sensing in structural health monitoring (SHM) refers to injecting (user-defined) energy into the system in order to actively probe its response to the induced dynamics as a means of detecting whether damage may be present in the system. A number of researchers have shown that active sensing with guided ultrasonic waves (GUWs) can be a powerful approach to take, as GUWs, when launched and detected in conjunction with macro-fiber composite (MFC) patches, can retain the wide area coverage capability of lower frequency (vibration) methods while significantly enhancing sensitivity to flaws (cracks, corrosion, etc.) because of the small interrogating wavelengths used.This project, led by PI Michael Todd and Co-PI Francesco Lanza di Scalea, considered several new concepts in guided GUWs: (i) optimized passive GUWs, (ii) quantitative active GUWs, and (iii) a generalized insonification (diffuse field) approach rooted in data-based modeling and pattern recognition. These concepts are tested on metallic test articles to detect a variety of defects, including impact damage, simulated cracks (notching), corrosion, and bolted joint preload loss.

15. SUBJECT TERMS
structural health monitoring, ultrasonic waves, insonification, wave propagation model

16. SECURITY CLASSIFICATION OF:			17. LIMITATION OF ABSTRACT	18. NUMBER OF PAGES	19a. NAME OF RESPONSIBLE PERSON
a. REPORT	b. ABSTRACT	c. THIS PAGE			Todd, Michael
U	U	U	SAR	39	19b. TELEPHONE NUMBER *(Include area code)* (858) 534-5951

ABSTRACT

Active sensing in structural health monitoring (SHM) refers to injecting (user-defined) energy into the system in order to actively probe its response to the induced dynamics as a means of detecting whether damage may be present in the system. A number of researchers have shown that active sensing with guided ultrasonic waves (GUWs) can be a powerful approach to take, as GUWs, when launched and detected in conjunction with macro-fiber composite (MFC) patches, can retain the wide area coverage capability of lower frequency (vibration) methods while significantly enhancing sensitivity to flaws (cracks, corrosion, etc.) because of the small interrogating wavelengths used.

This project, led by PI Michael Todd and Co-PI Francesco Lanza di Scalea, considered several new concepts in guided GUWs: (i) optimized passive GUWs, (ii) quantitative active GUWs, and (iii) a generalized insonification (diffuse field) approach rooted in data-based modeling and pattern recognition. These concepts are tested on metallic test articles to detect a variety of defects, including impact damage, simulated cracks (notching), corrosion, and bolted joint preload loss.

1. INTRODUCTION

The use of original design solutions and innovative materials in response to the evolving demands of the industry introduces challenges. In the naval industry, for example, there has been the development of high-speed and high-performance vessels. The aluminum material being considered for the newest Navy platforms is susceptible to stress corrosion cracking, fatigue cracking, or sudden failure due to the impact of waves or small icebergs, called bergy bits. Bolted connections in a number of structural components are also of interest.

Structural health monitoring solutions able to detect and quantify structural defects could be beneficial in these innovative naval structures providing information on the condition of the structure in real-time (Condition-Based Monitoring). Overall, the approach is an "active and passive sensing" approach whereby elastic waves are created and propagated through the hull, and features derived from the waves' interaction with the hull are mined for evidence of hull condition changes. While the passive approach is a form of acoustic emission whereby growing cracks are detected in real time, the active sensing approach is meant to detect and quantify both growing and stable cracks. Furthermore, a third form of elastic wave probing (in the active mode) that takes advantage of the diffuse, reverberant field (rather than explicit mode probes) is explored as a means of detecting and classifying defects.

In the passive approach, growing damage or sudden impacts can be located by monitoring acoustic emissions in a real-time mode (Mal *et al* 2005, Banerjee *et al* 2005, Prosser *et al* 1995). Traditionally, damage or impact location is based on time-of-flight triangulation of wave measurements taken at multiple receiving points. One problem with time-of-flight triangulation is the dispersive nature of the flexural mode which makes it difficult to identify an accurate arrival time from, for example, the conventional first-threshold crossing. This concern remains despite the proposed improvements over the first threshold crossing, such as cross-correlation techniques for extracting the phase of a single frequency component (Ziola and Gorman 1991). The measurement of the less dispersive extensional mode can theoretically help identifying a correct arrival time (Gorman and Ziola 1991). However, the extensional mode can be highly

attenuated in composites or generally large structures, in which cases triangulation of the flexural mode often remains the only realistic option. Another reason for preferential use of the (fundamental) flexural mode is the lower phase velocity compared to the (fundamental) extensional mode at the same frequency. This results in smaller wavelengths thus higher sensitivity to small damage. The second, more severe problem with time-of-flight triangulation is the required knowledge of the wave velocity in the test material. The velocity is required to translate arrival time measurements into source location. This requirement is a fundamental limitation when monitoring anisotropic or geometrically-complex structures (e.g. aerospace panels), where the velocity is dependent upon propagation direction. Model-based approaches (Chang and Markmiller 2006, Park and Chang 2005, Seydel and Chang 2001) have thus been required for impact location and identification in simple composite structures. In these methods the location and type of impact in a model are iteratively changed until the predicted responses match the measured responses. For damage/impact location in more complex structures, where accurate model-based predictions may not be possible, artificial neural networks have been proposed (Staszewski *et al* 2000, Jones *et al* 1997, Schindler *et al* 1995). However, neural networks require an extensive number of training observations prior to deployment, and they cannot provide deterministic locations. However all the works previously mentioned has focused on impact tests performed in a low velocity regime. In fact the actual impacts were generated using hand-held hammer, falling weight or just pencil lead breaks (Hsu-Nielsen). What are missing are investigations of impacts in a more realistic velocity regime. This paper presents experimental investigation of high velocity ice impacts location based on piezoelectric rosettes. Ice projectiles, were projected at velocity around 30 m/s using a gas-gun onto a 6061-T6 aluminum plate and a $[0/+45/90/-45]_S$ woven composite plate. The rosettes exploit the highly directional response of Macro Fiber Composite (MFC) rectangular patches to determine the direction of an incoming wave independently of the wave velocity in the medium. MFC patches, originally developed at NASA Langley Research Center for low-frequency structural control (Wilkie et al. 2000, Sodano et al. 2004), are recently being used for guided-wave transduction in aircraft structures owing to their superior flexibility and durability compared to monolithic PZTs (Lanza di Scalea et al. 2007a, Matt and Lanza di Scalea 2007, Salamone et.). Since no wave velocity information or complex modeling is required, the proposed technique can improve source location in anisotropic and geometrically-complex structures.The general idea of using rosettes for the detection of ultrasonic waves is not new. However, the use of piezoelectric rosettes for extracting the direction of incoming waves, thus allowing real-time source location, is novel. Recent works employing rosettes of Bragg grating fiber-optic strain sensors (Thursby *et al* 2004 and 2006) for wave direction determination. However, current technology for Bragg grating detection of ultrasound requires manual tuning of the laser to a high-sensitivity wavelength specific to each grating. Consequently, ultrasonic measurements cannot be taken from all three gratings of the rosette simultaneously, which limits the technique to locating existing defects only, rather than growing damage or impacts in real time. In addition, the periodicity of the Bragg grating response requires sophisticated data reduction steps, such as genetic algorithms (Thursby *et al* 2004), to identify univocally the wave incoming angle. These issues are avoided with piezoelectric, rather than optic, wave sensing. In a previous study (Matt and Lanza) the performance of the rosettes for source location was validated through pencil-lead breaks performed on an aluminum plate, an anisotropic CFRP laminate, and a complex CFRP-honeycomb sandwich panel. In this work, experimental results will be shown to demonstrate the applicability of this approach to a more realist impacts as ice projectiles.

In the active approach, guided waves are injected in a defected region, thereby inducing complex scattering. By studying the characteristics of the reflected and transmitted waves, quantitative information on the defects is obtained. Quantitative defect information can be extracted by using a hybrid formulation wherein the finite element method is used to model small regions near the defect whereas regions away from the defect are modeled using a suitable set of wave functions. Dong *et al* (2004) developed a global-local finite element formulation for modeling axisymmetric scattering of a steady, compressive, incident elastic wave in a homogeneous, isotropic host medium with an axisymmetric inclusion. The hybrid method was also used (Al-Nassar *et al* 1991, Rattanawangcharoen *et al* 1997) to model defects in a plate and a cylinder, respectively. The method has been applied to model wave interaction with defected lap-shear joints (Chang and Mal 1995), as well as notches and rivet-hole cracks in plates (Mal and Chang 2000, 1999). Doyle (Gopalakrishnan and Doyle 1995, Doyle 1995) employed a similar global-local scheme wherein the global field was modeled by using spectral elements.

Many components are complex in either their geometry (e.g. multilayers, tapered thickness, etc.) or their material properties (e.g. anisotropic). In this case theoretical wave solutions for the global portion are either nonexistent or hard to determine. The Semi Analytical Finite Element (SAFE) method can help handle these cases because of its ability to extract modal solutions of complex structures in a computationally efficient manner (Bartoli *et al* 2006, Hayashi *et al* 2003, Treyssede 2008, Castaings and Lowe 2008, Hayashi *et al* 2006, Al-Qahtani *et al* 2005, Lanza di Scalea *et al* 2007, Matt *et al* 2005). Sabra (Sabra *et al* 2008) demonstrated the application of the hybrid formulation to the detection of holes in aluminum plates. The present paper extends the global-local approach to model notches in aluminum plates and delamination-like defects in composite panels.

This previous active approach inherently relies upon characteristics of specific GUW modes and their properties, and the GUWs' interaction with the structure. When coupled with SAFE models, very specific features may be identified that can indicate specific flaws. However, structural geometries such as highly curved regions, bolted interfaces, etc., pose significant modeling and testing challenges for GUWs, resulting in difficulty in classifying size or type of damage due to the inherent simplicity of the actively imparted excitation signal, which is usually a modulated, narrow-band, short-wave pulse. Instead, some researchers have attempted to employ bulk insonification, where an ultrasonic source is excited, and the resultant long-time, or diffuse, wave field is examined to identify structural changes (Michaels and Michaels, 2005). This method is investigated as well to augment the standard guided wave method for structures with complex boundary conditions or geometries that make tracking and analysis of a single propagating mode difficult or impossible. This approach relies on data-driven (typically, time series) models and change detection approaches rooted in statistical pattern recognition.

Given these varied approaches, one might envision a possible general taxonomy for damage detection strategies in the ultrasonic domain as shown in Figure 1. SAFE (physics-based) modeling is critical for the middle column, and data-based modeling is critical for the right-hand column. This project presents studies that consider new ways how the structural health monitoring (SHM) "online" approaches can work for metallic structure defect detection, localization, and classification and form a complementary capability for Navy applications.

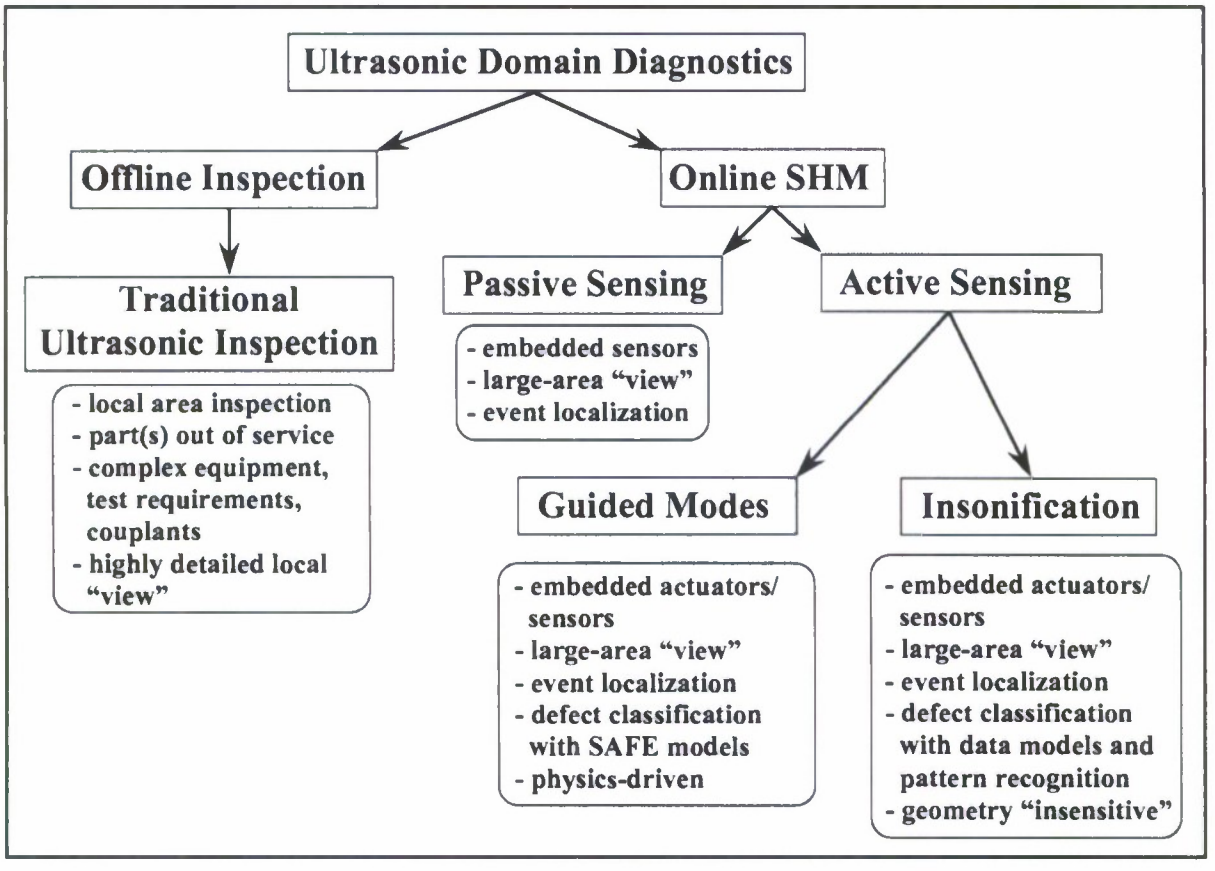

Figure 1 Ultrasonic domain diagnostic taxonomy.

2. PASSIVE APPROACH

2.1. Response Of Micro Fiber Composite To Flexural Lamb Waves

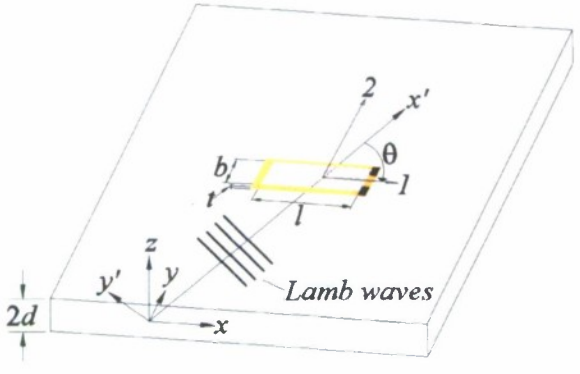

Figure 2 MFC geometry.

Consider a thin rectangular MFC transducer (type P2) acting as a sensor and having an effective length, *l*, width, *b*, and thickness, *t*, along the coordinates *1*, *2* and *3*, respectively (Figure 2). The Cartesian reference system (*x*, *y*, *z*) is aligned with the transducer's geometrical axes (*1*, *2*, *3*). This transducer is bonded to the upper surface of an isotropic plate of thickness 2*d* and subjected to a harmonic strain field associated to antisymmetric (flexural) Lamb waves propagating in the plane (*x'*, *z*) along direction *x'*. This wave mode is commonly used for the detection and location of damage or impacts,

as diseussed in the introduetion. The wave propagation direction x' forms an angle θ with the lengthwise direetion of the sensor. The origin of the thiekness eoordinate, $z = 0$, is at the mid-plane of the plate.

To derive the MFC sensor voltage response, in a previous work Matt et al. modeled it as an orthotropic lamina in plane stress conditions, and, considering the eleetrieal boundary eonditions of the MFC sensor to be an open eireuit, the following expression was obtained, ignoring shear lag effects:

$$V = iS\bar{\varepsilon}_{x'x'}e^{-i(\omega t+\frac{\pi}{2})} \tag{1}$$

where $\bar{\varepsilon}_{x'x'}$ is the amplitude spectrum of the surface strain defined as:

$$\bar{\varepsilon}_{x'x'} = k^2\left(\tanh rd - \frac{2rs}{k^2+s^2}\cdot\tanh sd\right) \tag{2}$$

and S is the frequency-dependent sensitivity faetor that, for antisymmetrie waves is:

$$S = \frac{4H}{lbk^2\sin\theta\cos\theta}\sin\left(\frac{kb\sin\theta}{2}\right)\sin\left(\frac{kl\cos\theta}{2}\right) \tag{3}$$

H is a frequency-independent constant depending on the in-plane orthotropic elastic constants (E_i, ν_{ij}), the electro-mechanical properties (e_{33}^{σ}, d_{31}, d_{32}), and thickness of the sensor (t), as well as on the wave propagation direction relative to the sensor geometrieal axes:

$$H = \frac{t\left[\left(d_{31}E_1 + d_{32}\nu_{12}E_2\right)\cos^2\theta + \left(d_{31}\nu_{12}E_2 + d_{32}E_2\right)\sin^2\theta\right]}{\left[\left(1-\nu_{21}\nu_{12}\right)e_{33}^{\sigma} - \left(d_{31}^2E_1 + 2d_{31}d_{32}\nu_{12}E_2 + d_{32}^2E_2\right)\right]} \tag{4}$$

The terms d_{32} d_{31} and e_{33}^{σ} are the piczoelectric constants and dielectric permittivity, respectively. In this expression, obtained under the assumption of plain waves ($\varepsilon_{y'y'} = 0$), the parameters r and s are defined as:

$$r = \sqrt{k^2 - \frac{\omega^2}{c_L^{\,2}}}, \qquad s = \sqrt{k^2 - \frac{\omega^2}{c_T^{\,2}}} \tag{5}$$

where ω is the frequency, k is the wavenumber, and c_L and c_T are the bulk longitudinal and shear velocities in the plate, respectively. Matt. Et al. demonstrated that the sensor behaves as an ideal strain deteetor when it is small compared to the wavelength (i.e. at lower frequeneies). At higher frequencies, where the wavelength is comparable to the sensor's dimensions, tuning effects, govern the response. It can be demonstrated that for $\lambda \geq l$ (sensor smaller than wavelength), the sensitivity can be decomposed into a longitudinal sensitivity faetor, S_1 , and a transverse

sensitivity factor, S_2, as:

$$S \approx S_1 \cos^2\theta + S_2 \sin^2\theta \tag{6}$$

where θ is the usual wave propagation direction relative to the sensor's lengthwise direction. The longitudinal and transverse sensitivity factors are defined for waves propagating along the sensor's lengthwise and widthwise directions, respectively. Thus:

$$\begin{aligned} S_1 &= S\big|_{\theta=0^\circ} = \frac{2t\left(d_{31}E_1 + d_{32}\nu_{12}E_2\right)\sin\left(kl/2\right)}{lk\left[\left(1-\nu_{21}\nu_{12}\right)e_{33}^{\sigma} - \left(d_{31}^2E_1 + 2d_{31}d_{32}\nu_{12}E_2 + d_{32}^2E_2\right)\right]} \\ S_2 &= S\big|_{\theta=90^\circ} = \frac{2t\left(d_{31}\nu_{12}E_2 + d_{32}E_2\right)\sin\left(kb/2\right)}{bk\left[\left(1-\nu_{21}\nu_{12}\right)e_{33}^{\sigma} - \left(d_{31}^2E_1 + 2d_{31}d_{32}\nu_{12}E_2 + d_{32}^2E_2\right)\right]} \end{aligned} \tag{7}$$

By substituting Eq. (6) into Eq. (1) and transforming the amplitude spectrum of the surface strain $\bar{\varepsilon}_{x'x'}$ into the lengthwise and widthwise axes of the sensor using the following strain transformation:

$$\begin{aligned} \varepsilon_{11} &= \bar{\varepsilon}_{x'x'}\cos^2\theta \\ \varepsilon_{22} &= \bar{\varepsilon}_{x'x'}\sin^2\theta \end{aligned} \tag{8}$$

the sensor's response becomes:

$$\bar{V} \approx S_1\,\bar{\varepsilon}_{11} + S_2\,\bar{\varepsilon}_{22} \tag{9}$$

where the wave strain components along the longitudinal and the transverse sensor directions are explicitly indicated. Eq. (9) makes the MFC response formally equivalent to that of conventional electrical resistance strain gages. This equation also emphasizes that the response is highly dependent on the wave propagation direction, and thus significant directivity behavior is expected at certain frequencies.

2.2. MFC Rosettes For Wave Source Location

Let us consider three rectangular MFC sensors *A*, *B* and *C* arranged in an arbitrary rosette configuration and subjected to antisymmetric waves as shown in Fig. 2a. Considering waves such that $\lambda \geq l$ and using Eq. (9), the sensors responses can be written as:

$$\begin{aligned} \bar{V}^A &= S_1\bar{\varepsilon}_{11}^A + S_2\bar{\varepsilon}_{22}^A \\ \bar{V}^B &= S_1\bar{\varepsilon}_{11}^B + S_2\bar{\varepsilon}_{22}^B \\ \bar{V}^C &= S_1\bar{\varepsilon}_{11}^C + S_2\bar{\varepsilon}_{22}^C \end{aligned} \tag{10}$$

where $\bar{\varepsilon}_{11}^{i}$ and $\bar{\varepsilon}_{22}^{i}$ (i =A, B, C) indicate, respectively, the strain components in the longitudinal and in the transverse direction of the i-th sensor, and all sensors are assumed equal in electro-mechanical and geometrical properties.

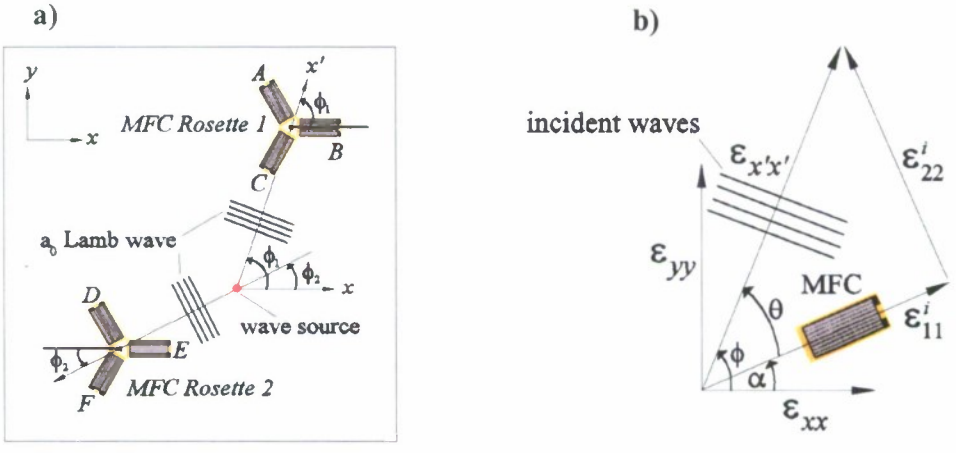

Figure 3 MFC rosette geometry.

Dividing Eq. (10) by the longitudinal sensitivity factor yields:

$$\frac{\bar{V}^{i}}{S_1} = \bar{\varepsilon}_{11}^{i} + K_T \bar{\varepsilon}_{22}^{i} \qquad \text{for } i = A, B, C \tag{11}$$

where K_T is a transverse sensitivity ratio defined as:

$$K_T = \frac{S_2}{S_1} = \frac{l\left(d_{31}\nu_{12}E_2 + d_{32}E_2\right)\sin\left(kb/2\right)}{b\left(d_{31}E_1 + d_{32}\nu_{12}E_2\right)\sin\left(kl/2\right)} \tag{12}$$

Let us assume that the lengthwise direction of the i-th sensor is oriented at an angle α_i from the global coordinate axis x. In analogy with electrical resistance strain gages, given the measurement of three independent strain from the response of the three sensors it is possible to calculate the Cartesian strain components and their principal strain angle ϕ. The principal strain angle of the wave, ϕ, measured from the global axis x (Figure 3a), can be computed as:

$$\tan 2\phi = \frac{\bar{\gamma}_{xy}}{\bar{\varepsilon}_{xx} - \bar{\varepsilon}_{yy}} \tag{13}$$

Evaluation of the source location in a plane is readily achieved by the intersection of the principal directions determined by two rosettes (Figure 3b). The principal angles calculated from

the two rosettes, ϕ_1 and ϕ_2, define the equations of the straight lines connecting the wave source to each of the rosette centroids according to:

$$y_{SOURCE} = (x_{SOURCE} - x_1)\tan\phi_1 + y_1$$
$$y_{SOURCE} = (x_{SOURCE} - x_2)\tan\phi_2 + y_2 \quad (14)$$

where (x_{SOURCE}, y_{SOURCE}) represent the coordinates of the wave source in the (x, y) Cartesian system, and (x_1, y_1), (x_2, y_2) represent the coordinates of the centroids of the two rosettes, respectively. The linear system of equations can finally be solved for the coordinates of the wave source:

$$x_{SOURCE} = \frac{y_2 - y_1 + x_1\tan\phi_1 - x_2\tan\phi_2}{\tan\phi_1 - \tan\phi_2}$$
$$y_{SOURCE} = (x_{SOURCE} - x_1)\tan\phi_1 + y_1 \quad (15)$$

2.3. Experiments

In a previous work, Lanza di Scalea et al., in collaboration with Dr. Hyonny Kim, studied impact location by using two rosettes attached to isotropic and CFRP anisotropic specimens, in a low velocity regime (pencil-lead breaks). To demonstrate the potential of this technique, source location was attempted in the high velocity regime. A nitrogen gas cannon (Figure 4), was used to shoot simulated hail ice (SHI) spheres. The monolithic ice spheres had a diameter of 38 mm and were cast in a split spherical mold over 1 filling session.

Figure 4 Gas gun for high-velocity impacts.

The specimen used for the validation test, shown in, consist of the 0.91 m × 0.91 m × 2.5 mm 6061-T6 aluminum plate. Two, three-element P-2 MFC rosettes, each arranged in a delta configuration (120° between adjacent sensors – Figure 6), were surface-bonded to the specimen. During testing, the Fast-Fourier Transform was performed for the time history of each sensor. The amplitude was computed in a narrow frequency band, near the point $\lambda = l$. For anisotropic structures, the frequency at which $\lambda = l$ is clearly direction dependent. Therefore the response magnitude was computed at the maximum frequency such that optimal directivity response was ensured while meeting the requirement $\lambda \geq l$ for all sensors within a rosette.

A typical signal captured from impact tests on the 6061-T6 aluminum plate is shown in Figure 5. The flexural anti symmetric A_0 mode component of this signal is clearly identified. This is expected since the impact produces a large out-of-plane flexural motion.

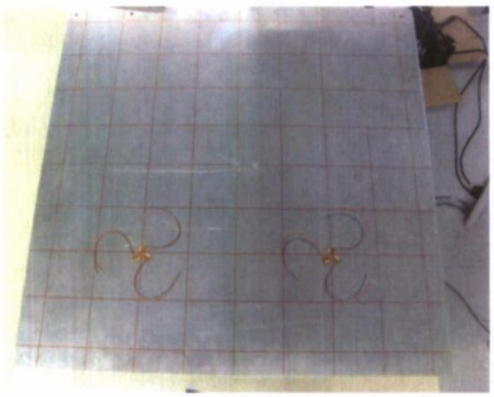

Figure 5 Aluminum plate used in impact study.

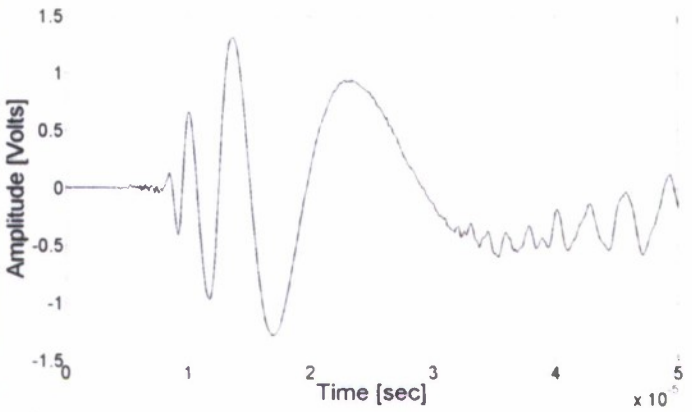

Figure 6 Typical recorded trace from impact.

The estimated impact speed was ≈30 m/s. The estimated impact locations results are shown in Figure 7 (right). In particular, Figure 7(left) shows a single frame extracted from a high-speed film taken during the impact test. As seen in the picture, the ice sphere locally crashes on the plate center. This actual impact location is marked in Figure 7(right) as a red circle. The predicted impact location, using the proposed method, is represented on the figure by a green circle. An RMS error function was defined to provide a measure of the rosettes performance; the RMS error is expressed as:

$$RMS = \frac{1}{n}\sqrt{\sum_{i=1}^{n}\left(x_{a,i} - x_{p,i}\right)^2 + \left(y_{a,i} - y_{p,i}\right)^2} \tag{16}$$

where n is the number of the test impacts, $(x_{a,i}, y_{a,i})$ are the coordinates of the actual impacts on the aluminum plate in millimeters and $(x_{p,i}, y_{p,i})$ are the coordinates of the predicted impact locations in millimeters. This form of the RMS error function gives the radial error (i.e., the vector length from the actual to the computed impact location). The estimated RMS error for this test was 18 radial mm.

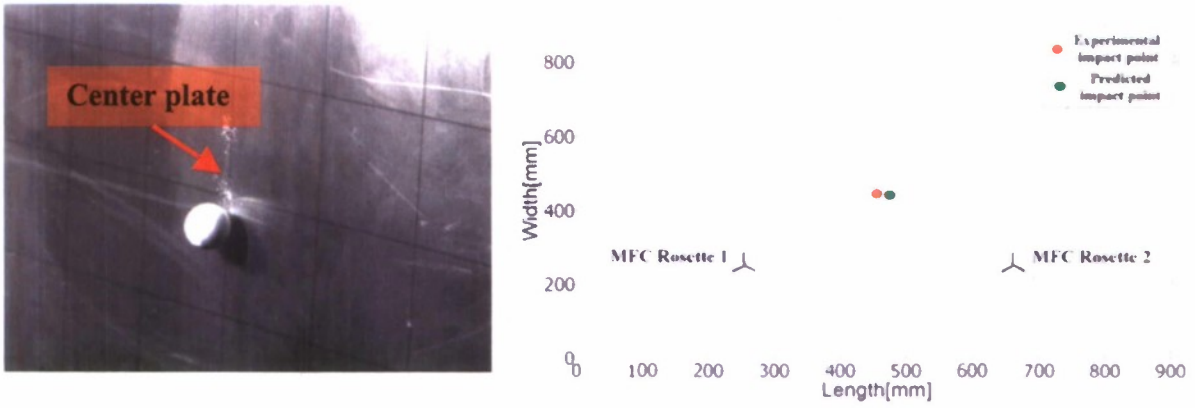

Figure 7 (left) High-speed imagery during impact test, and (right) comparison of predicted and actual impact location.

3. ACTIVE APPROACH: EXPERIMENTS AND MODELING USING GUIDED MODES

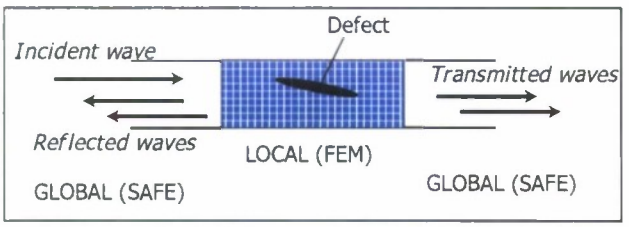

Figure 8 Schematic of global-local approach.

The geometry of the problem at hand is depicted in Figure 8, where the material inside the bounded surface has properties different from the outside due to the presence of local irregularities as a defect. In order to best illustrate this hybrid method, assume that a plane time-harmonic wave is incident on the FEM boundary in Figure 8. The region inside the boundary is meshed and analyzed using standard finite element analysis; the region outside the boundary is represented by the linear combination of a set of global wave functions, here calculated from the SAFE method. The continuity of displacements and tractions on the mesh boundary must be satisfied through proper choice of the amplitudes of the wave functions.

3.1. Semi-Analytical Finite Element Method

The SAFE method is employed to calculate the guided wave modeshapes Φ and eigenvalues ξ for any infinitely-uniform cross-section. These modeshapes and eigenvalues are used to calculate the forces and displacements on the boundary separating the Global from the Local region. In the SAFE method, at each frequency ω a discrete number of guided modes is obtained.

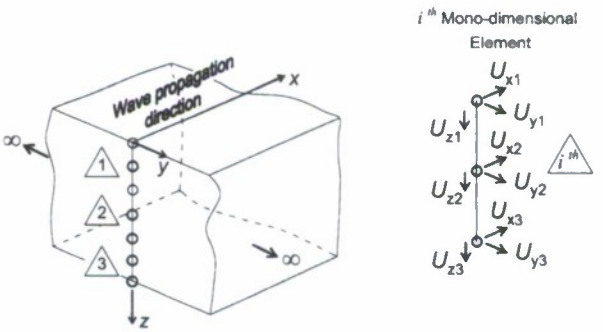

Figure 9 Discretization in the semi-analytical finite element method.

For the given frequency, each mode is characterized by a wavenumber, ξ, and by a displacement distribution over the cross-section. For a Cartesian reference system, the waveguide cross-section is set in the y-z plane while the x-axis is parallel to the waveguide length (Figure 9).

Subdividing the cross-section via finite elements, the approximated displacement at a point, $u = u(x, y, z, t)$, is given as:

$$u = N U^e e^{j(\xi x - \omega t)} \tag{17}$$

where $N = N(y, z)$ is the matrix of the shape functions, U^e is the nodal displacement vector for the e-th element, t is the time variable and i the imaginary unit. It can be noted that the displacement is described by the product of an approximated finite element field over the waveguide cross-section with exact time harmonic functions, $e^{i(\xi x - \omega t)}$, in the propagation direction, x. The compatibility and constitutive equations can be written in synthetic matrix forms as:

$$\varepsilon = Du \qquad \sigma = C^* \varepsilon \tag{18}$$

where ε and σ are the strain and stress vectors respectively, D is the compatibility operator and C^* is the stiffness tensor which is general can be complex (viscoelastic behavior). More details on the compatibility operator can be found in (Gopalakrishnan and Doyle 1995) and (Doyle 1995). The principle of virtual work with the compatibility and constitutive laws, Eqs.(17) and (18), leads to the following energy balance equation

$$\int \delta u^T \tau d\Gamma = \int \delta u^T (\rho \ddot{u}) dV + \int \delta (uD)^T C^* D u dV \tag{19}$$

where Γ is the waveguide cross-section area, V is the waveguide volume, τ is the external traction vector and the overdot means time derivative. The finite element procedure reduces Eq.(19) to the set of algebraic equations:

$$\left[A - \xi B\right]_{2M} \Phi = p \tag{20}$$

where the subscript $2M$ indicates the dimension of the problem with M the number of total degrees of freedom of the cross-sectional mesh. Details on the complex matrices A and B can be found in Hayashi *et al* 2003. By setting p=0 in Eq.(20), the associated eigenvalue problem can be solved as $\xi(\omega)$ which gives the wavenumbers for the different Lamb modes of the structure at frequency ω. For each frequency ω, $2M$ complex eigenvalues ξ_m and $2M$ complex eigenvectors Φ_m are obtained. The solution is symmetric, i.e. for each pair (ξ_m, Φ_m), representing a forward guided mode, a pair exists representing the corresponding backforward mode. The first M components of Φ_m describe the cross-sectional mode shapes of the m-th mode. Once ξ_m is known, the dispersion curves can be easily computed. The phase velocity can be evaluated by the expression $c_{ph} = \omega / \xi_{real}$, where ξ_{real} is the real part of the wavenumber. The imaginary part of the wavenumber is the attenuation, att=ξ_{imag}, in Nepers per meter.

3.2. Global-Local Method

The global functions, represented by Φ_n, are the displacements that satisfy the governing equations in the absence of the discontinuity. The displacements at the mesh boundary are written as a sum of the contribution due to the incident wave and that due to the scattered waves. This displacement is then further used to satisfy the continuity conditions at the boundary.

The displacements at the left boundary are written as:

$$u_l = u_{incident} + u_{scattered}$$

$$A_{in} \Phi^+_{in} e^{i\left(-\xi^+_{in} x^-\right)} + \sum_{j=1}^{L} A^-_j \Phi^-_j e^{i\left(-\xi^-_j x^-\right)} \tag{21a}$$

$$u_l = A_{in}\Phi^+_{in}e^{i\left(-\xi^+_{in}x^-\right)} + \left[G^-\right]\left[D^-\right] \tag{21b}$$

where the time-harmonic dependence is implicit.

Rattanawangcharoen *et al* (1997) gives a detailed description of matrices $\left[G^-\right]$,$\left[D^-\right]$. In essence, $\left[G^-\right]$ is a matrix consisting of the modeshapes of the scattered modes whereas $\left[D^-\right]$ is a column vector which contains the resultant displacement due to these modes on the left boundary.

In equations (21a, 21b), Φ^+ represents the modeshape of the incident waves travelling to the right, Φ^- represents the modeshapes of the reflected waves travelling to the left; A_{in}, Φ^+_{in}, and ξ^+_{in} represent the amplitude, modeshape and wavenumber of the incident wave respectively; A^-_j represents the unknown amplitude of the reflected waves; superscript '+' represents a wave travelling in the right and a superscript '-' represents a wave travelling in the left direction; x^- represents the absolute value of the distance of the left boundary from the center of the meshed region; L is the total number of modes considered. In the same way, the displacements at the right boundary are written as:

$$u_l = u_{incident} + u_{scattered}$$

$$A_{in}\Phi^+_{in}e^{i\left(\xi^+_{in}x^+\right)} + \sum_{j=1}^{L} A^+_j\Phi^+_j e^{i\left(\xi^+_j x^+\right)} \tag{22a}$$

$$u_r = A_{in}\Phi^+_{in}e^{i\left(\xi^+_{in}x^+\right)} + \left[G^+\right]\left[D^+\right] \tag{22b}$$

In equations (22a)-(22b), A^+_j represents the unknown amplitude of the transmitted waves and x^+ represents the absolute value of the distance of the right boundary from the center of the meshed region.

The forces at the boundaries can be calculated by computing the consistent nodal force vectors due to displacements (21b) and (22b). The nodal forces at the left boundary are:

$$f_l = -A_{in}F^+_{in}e^{i\left(-\xi^+_{in}x^-\right)} + \left[F^-\right]\left[D^-\right] \tag{23}$$

F_j is the consistent nodal force vector calculated from the displacement vector Φ_j. The nodal forces at the right boundary are:

$$f_r = -A_{in}F^+_{in}e^{i\left(\xi^+_{in}x^+\right)} + \left[F^+\right]\left[D^+\right] \tag{24}$$

3.3. Finite Element Model for Local Region

The conventional discretization process in the finite element method yields:

$$\delta\{q^*\}[S]\{q\}-\delta\{q_B^*\}\{P_B\}=0 \tag{25a}$$

$$[S]=[K]-\omega^2[M]=\begin{bmatrix} S_{II} & S_{IB} \\ S_{BI} & S_{BB} \end{bmatrix} \tag{25b}$$

$$\{q\}^T=\left\langle \{q_I\}^T \{q_B\}^T \right\rangle \tag{25c}$$

Here, $[K]$, and $[M]$ are global stiffness and mass matrices respectively; ω is the harmonic frequency; $\{q_I\}$ and $\{q_B\}$ are the nodal displacement vectors corresponding to interior and boundary nodes respectively; $\{P_B\}$ is the interaction force vector at the boundary nodes; and $\{q^*\}$ denotes complex conjugate of $\{q\}$. Forces on the boundary nodes due to the entire FE region, when displacement is imposed only on the boundaries, can be calculated by performing static condensation on $[S]$ such that:

$$\left[S_{BB}^*\right]=[S_{BB}]-[S_{BI}][S_{II}]^{-1}[S_{IB}] \tag{26}$$

3.4. Global Solution

The nodal forces on the boundary due to displacements (21b) and (21b), as contributed from the FE portion, are:

$$f_{boundary}^{FEM}=\left[S_{BB}^*\right]\begin{Bmatrix}\{u_l\}\\ \{u_r\}\end{Bmatrix} \tag{27}$$

For traction continuity, from equations (21), (22), and (27):

$$\begin{Bmatrix}\{f_l\}\\ \{f_r\}\end{Bmatrix}=f_{boundary}^{FEM}=\left[S_{BB}^*\right]\begin{Bmatrix}\{u_l\}\\ \{u_r\}\end{Bmatrix} \tag{28}$$

Rearranging the terms, the following final equation is obtained:

$$\left(\left[S^*_{BB}\right][G]-[F]\right)\{D\}=\left\{P^B_{in}\right\}-\left[S^*_{BB}\right]\left\{q^B_{in}\right\} \tag{29a}$$

$$\left\{P^B_{in}\right\}=\begin{Bmatrix} A_{in}F^+_{in}e^{i\left(-\xi_{in}x^-\right)} \\ A_{in}F^+_{in}e^{i\left(\xi_{in}x^+\right)} \end{Bmatrix} \tag{29b}$$

$$\left\{q^B_{in}\right\}=\begin{Bmatrix} A_{in}\Phi^+_{in}e^{i\left(-\xi_{in}x^-\right)} \\ A_{in}\Phi^+_{in}e^{i\left(\xi_{in}x^+\right)} \end{Bmatrix} \tag{29c}$$

$$\{D\}^T=\left\langle\left\{D^-\right\}^T\left\{D^+\right\}^T\right\rangle \tag{29d}$$

$$[F]=\begin{bmatrix}\left[F^-\right] & 0 \\ 0 & \left[F^+\right]\end{bmatrix} \tag{29e}$$

$$[G]=\begin{bmatrix}\left[G^-\right] & 0 \\ 0 & \left[G^+\right]\end{bmatrix} \tag{29f}$$

Equation (29a) is solved using least squares to calculate the coefficients A^-_j, and A^+_j. Reflection coefficients (R_{ij}) and transmission coefficients (T_{ij}) (due to the i[th] incident mode) are defined below:

$$R_{ij}=A^-_j/A_i \tag{30}$$

$$T_{ij}=\begin{cases} A^+_j/A_i\,;\ j\neq i, \\ 1+A^+_j/A_i\,;\ j=i \end{cases} \tag{31}$$

3.5 Energy Conservation

Energies are carried only by the propagating modes, which include incident, reflected and transmitted modes. The time averaged values of energy flux associated with the j[th] reflected and transmitted modes through the cross-section is given by:

$$I_{ij}^{-} = \omega |A_i|^2 |R_{ij}|^2 \alpha_j \qquad (32)$$
$$I_{ij}^{+} = \omega |A_i|^2 |T_{ij}|^2 \alpha_j$$

where

$$\alpha_j = \left[\int_0^h F_j^{+} \bar{q}_j z dz \right] \qquad (33)$$

is the participation factor for the j[th] propagating mode and the integration is carried over the thickness of the plate (h).

3.6. Numerical Results And Experimental Comparisons

3.6.1. Reflection for Notched Aluminum Plate

This study examined a semi-infinite plate with a notch defect. The plate modeled was aluminum, 1.58 mm (1/16 in) in thickness. The first notch considered was 0.16 mm in width and 0.32 mm in depth (Figure 10(top)). A finite region surrounding the notch (local domain) was discretized by rectangular, four-node finite elements. A total of ten elements were used in the thickness of the plate, and the mesh was kept uniform throughout the local domain. SAFE was used for the global domain. The zero-order symmetric mode, S_0, was considered as the incident mode.

The results are shown in the plot of Figure 10(top) in terms of reflected energy relative to the incident, unit energy. As expected, the notch causes S_0-A_0 mode conversion since it breaks the symmetry of the waveguide. As a check for the accuracy of the analysis, energy conservation is preserved as the reflected S_0 and A_0 energies sum to the incident S_0 energy. Mode conversion is found more pronounced at particular frequency values, namely 500 kHz, 730 kHz, 880 kHz and 950 kHz.

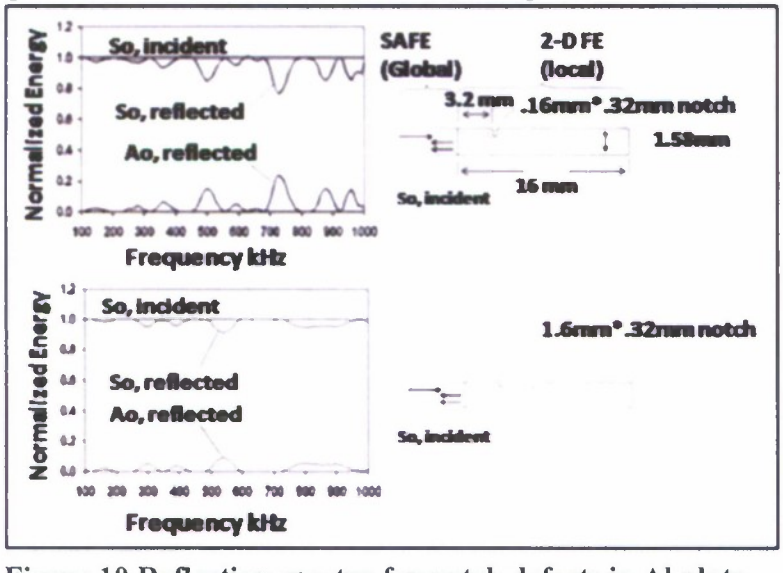

Figure 10 Reflection spectra for notch defects in Al plate.

A more shallow discontinuity was examined next. This was a notch extending 1.6 mm in width and 0.16 mm in depth, which more closely represented corrosion damage (Figure 10(bottom)). It can be seen that the resulting reflection spectra are different for the two defect cases. This suggests the potential for quantitative, rather than qualitative defect detection.

3.6.2. Reflection and Transmission for Notched Aluminum Plate

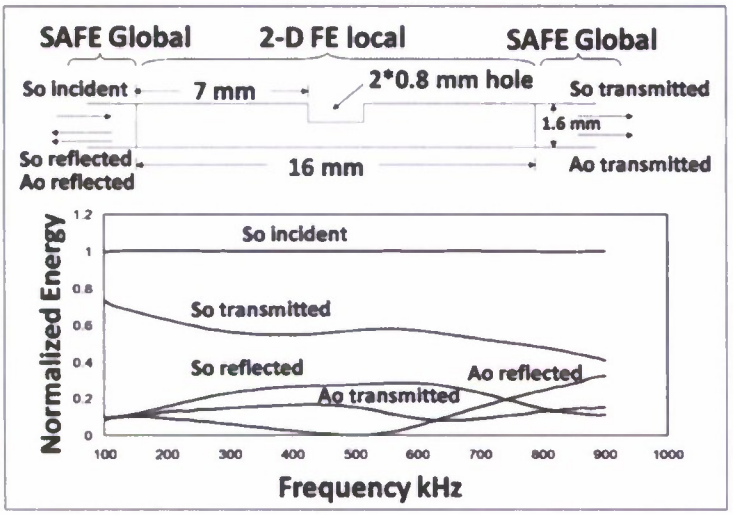

Figure 11 Reflection and transmission spectra for notch defects in an Al plate.

In this case the global-local method was used to predict the scattered field in both reflection and transmission. The plate modeled was aluminum, 1.6 mm in thickness with a half thickness notch in the middle. Transmitted and reflected S_0 and A_0 modes were computed for an incident S_0 mode. Energy conservation was again checked to test the validity of the method (Figure 11).

3.6.3. Time Histories

The global-local method was also used to predict the time-domain waveforms in an aluminum plate subjected to broadband, pulsed laser excitation. The response was experimentally measured for the case of a plate 1.58 mm in thickness with a sensor-excitation distance of 20 cm. Figure 12(a) shows the geometry of the problem. Figure 12(b) and Figure 12(c) show the comparison of the theoretical predictions with experimentally measured results. The numerical predictions were calculated by inverting the frequency response calculated from the SAFE-based global-local method.

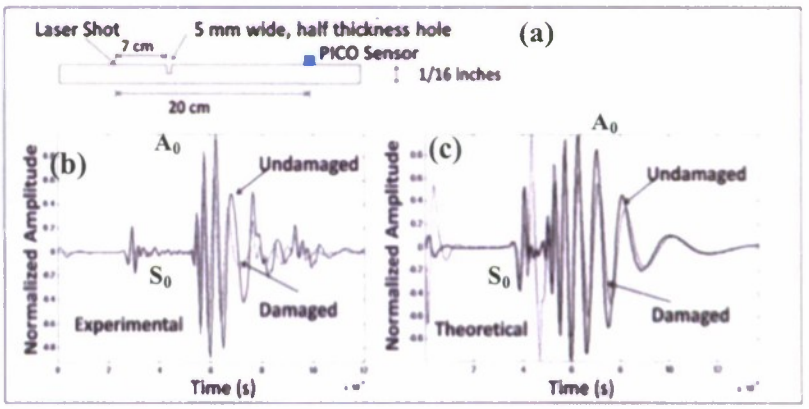

Figure 12 Time histories for notched Al plate: experiments and simulations.

It can be seen that a small discrepancy exists between the model and the experiment in the wave arrival time of S_0, whereas good match is found for A_0. The S_0 discrepancy may be due to an imperfect knowledge of the material in the test. It is nevertheless worth noting that both the numerical predictions and the experimental results show a decrease in the amplitude of the A_0 mode in the case of the notched plate. The numerical prediction also shows significantly more mode conversion when compared to the experimental results. This is primarily because of energy conservation concerns for the plain strain approximation of a three dimensional problem. While energy is allowed to scatter in random directions in the experimental case, reducing the problem to 2

dimensions forees the seattered energy from the A_0 mode to be transferred to the S_0 mode. Further studies, including adding higher-order scattered modes, refining the finite element mesh, and extending the 2-D global-local formulation to 3-D, are being conducted to obtain a better convergence of the model with the experiments.

4. INSONIFICATION APPROACH

4.1. Chaotically-modulated Insonification and Time Series Predictive Modeling

These GUW teehniques are well established and can work in certain structures with simple geometries (e.g., plates, beams, ete.) or on sections with eonstant cross-seetion properties in the wave propagation direetion (e.g., rails). However, these methods eannot as easily be applied to irregular geometries, sueh as bolted joints, stiffened ribs, or curve panels, beeause of mode conversion and wave interferenee effects that arise as a result of the complex interfaces and mechanical impedanee mismatches in these constructions. Instead, some researchers have attempted to employ bulk insonifieation, where an ultrasonic source is excited and the resultant long-time, or diffuse, wave field is examined to identify struetural changes (Miehaels and Michaels, 2005). This method is complementary to GUW mode-locked analyses for structures with complex boundary eonditions or geometries that make traeking and analysis of a single propagating mode difficult or impossible.

The new approach created here uses a ehaotieally-modulated ultrasonie wave as the probe. Methods that employ ehaotic excitations and attractor-based prediction error algorithms (but not in the ultrasonie domain) have demonstrated the eapaeity to deteet defeets in various test bed structures with enhanced sensitivity over traditional vibration-domain analyses (Nichols, Todd and Wait, 2003; Todd, Erickson, Chang, Lee and Niehols, 2004). The key lies in the phase-space diversity of the chaotic sideband structure. Dispersion issues are less important, as the primary point is to use the phase-diverse (chaotic) waveform as a eonstant probe souree and employ some form of waveform eomparison or time series predictive model to contrast a "baseline" condition with a test eondition. The ehaotie ultrasonic waves are fundamentally created via amplitude modulation, i.e., by multiplying a single ultrasonic frequency tone by an amplitude envelope that is created by a separate chaotic process. A chaotic waveform is able to enhance prediction error based features beeause the signal is deterministic; it is not just frequency strueture that's important. Using a phase-randomized signal with frequeney content equivalent to a chaotic waveform results in extracted features that are not able to identify damage as well as deterministic chaotic waveforms (Niehols, Todd and Wait, 2003). The waveform appears as a narrowband, chaotically-modulated signal centered at some central carrier frequeney. Although not required, it is usually best to select a carrier frequency where dispersion is still somewhat minimal relatively minor dispersion that oeeurs in aluminum at that frequency (although this is not a requirement), beeause of the bar thickness that is used in the experimental study, and beeause the traveling modes are well-separated in phase velocity space.

Creation of this signal is a multi-step proeess and starts with the generation of a 1 Hz sine wave with a time step $dt=1/f_s$, where f_s is the sampling frequency (chosen to be 4 MHz for experimental investigation below due to data acquisition limitations). A 1 Hz sine wave is used because a standard Lorenz chaotic signal has significant frequency information only in the 1 Hz

range and therefore when the ehaotie signal is used to window the sine wave they have similar frequeney eontent. At the end of the windowing proeess the new windowed chaotic signal ean then be shifted to thc desired center frequency by changing the size of the time step used in the time vector. The chaotic signal is constructed using the output of the x variable from the following three-dimensional nonlinear Lorenz system:

$$\dot{x} = 10(y - x)$$
$$\dot{y} = (-xz + 28x - y)$$
$$\dot{z} = (xy - 8z/3) \tag{34}$$

There is nothing unique about the Lorenz system for generating chaotic output; any system capable of producing a chaotic output is suitable, but the Lorenz system shown in (34) has a robust parameter region for produeing chaotie output and was selceted for this study. Equation (34) is integrated using a time-step $dt*R$, where R is a frequency ratio that can be modified to change thc frcqueney bandwidth of the ehaotie signal. For this study we use several values of R which affect the frequency regime in whieh the power of the chaotic signal lies. For example, a value of R=1/3 ereates a signal in whieh the signifieant frequency information (as determined by a loss of 40 dB in power spectral density) is less than 1.5 Hz. A value of R=1/30 would result in significant frequency information being less than 0.2 Hz. This chaotie signal is normalized through division by the maximum of the absolute value of the signal so that the values range from -1 to 1. A modulated signal is then created using the following equation:

$$\mathbf{y} = \sin(2\pi * \mathbf{t}) * (1 + d * \mathbf{x}) \tag{35}$$

where $\mathbf{x}$ is the Lorenz waveform, $\sin(2\pi*t)$ is the originally created sine wave, d is the modulation depth, and $\mathbf{y}$ is the chaotically amplitude-modulated output signal. If the value of d, whieh eontrols signal bandwidth, is greater than one, the resulting signal will be over-modulated and will result in a phase inversion at the points where $|d*\mathbf{x}|>1$. These phase inversions would be detrimental to any predietion algorithm, and d is therefore restricted to the range $0<d\leq 1$. The amplitude modulated signal is then upconverted to the target earrier wave frequency by multiplying $dt*f_c$. The resulting ehaotie time series are also smoothed in time at its boundaries with a trapezoidal window to facilitate launching with piezoelectric devices. The CUWs were launched over a 2 ms time period. Figure 13 depicts the actual time series for various parameter combinations, and Figurc 14 shows the effect of changing the frequeney ratio R as well as the modulation depth d on thc power spectral density of the modulatcd carrier wave. The effectiveness of the damage deteetion technique used in this study is highly dependent on carrier frequency and frequency ratio but appears to bc relatively insensitive to modulation depth, provided a value significantly larger than zero is used (Fasel, Olson, and Todd, 2008).

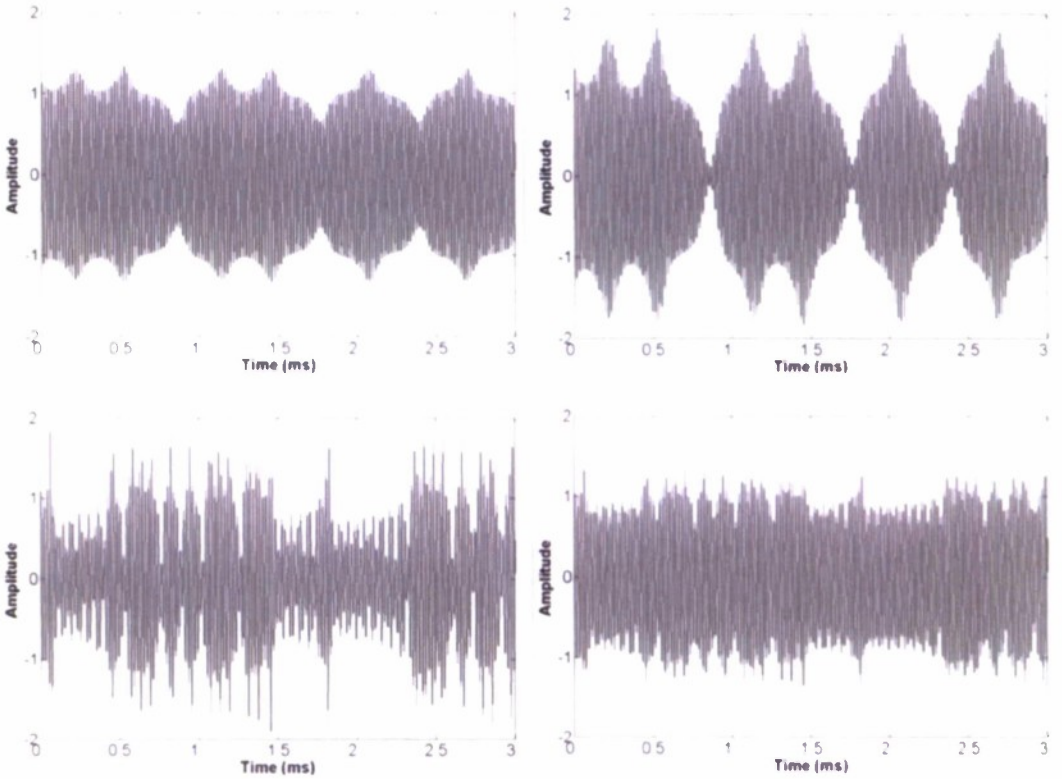

Figure 13 Modulated signals using (top left) $R = 0.10$ and $d = 0.5$; (top right) $R = 0.10$ and $d = 1.0$; (bottom left) $R = 0.33$ and $d = 0.5$; (bottom right) $R = 0.33$ and $d = 1.0$.

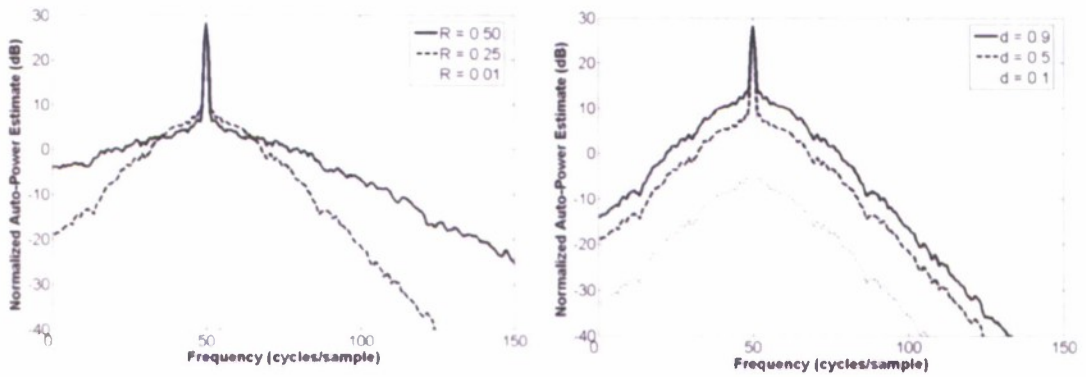

Figure 14 (left) Power spectral densities of modulated signals using d=0.5 and (right) power spectral densities of modulated signals using R=0.33.

Once the CUW has been created it is then imparted to the structure through an MFC (or similar piezoelectric) sensor/actuator, the characteristics of which were described in Section 2. The waveform is detected by a second sensing MFC in a pitch/catch mode. The primary task at this point in the damage detection scheme is to decide what feature(s) from the measured waveform

may be extraeted to best assess the eondition status of the strueture. A novel statistieal elassifieation teehnique with its basis in information theory is employed for this study.

A fundamental theorem of Shannon's information theory says, paraphrased intuitivcly, "the best eompression for any given data set comes from a codebook designed exactly for the statisties of that souree, any other eodebook will give worse results" (Shannon and Weaver, 1949). For instance, if one has a codebook (e.g., taking language elements like words into shorter eodes) consisting of English words and another eonsisting of French words, then a new time series of letters ean be represented in the shortest compressed format when using the English eodebook versus all others if the new text is, in faet, written in English. Compression performanee is the elassie text eategorization methodology. Modern statisties has melded ideas of information theory to extend to continuous signals, where compression performanee is intimately tied with out-of-sample prediction error, and a codebook is the model for a souree (something that produees time series data). In this ease the souree arises from an actual physieal proeess (the guided wave propagating through a bolted joint). This idea leads to a proeedure for elassifying time series using eross-prediction error, as literal "data eompression" is not aetually neeessary, just its "virtual" performance. First, a suitable model of the measured response time series is required, as opposed to the eomputationally-intensive, first-prineiples physieal spatially-extended finite element model of the joint. The perfect model for elassifieation is not needed, as it can work well with reasonable model misspeeifieation. However, the better the underlying statistieal model is, of course, the more the elassifieation performanee will improve.

The first step in this method employs the use of autoregressive (AR) models, which have previously been shown to be useful in damage classification schemes (Sohn and Farrar, 2001; Sohn, Farrar, Hunter and Worden, 2001). The diseretely observed output time series $\boldsymbol{x}(n)$ is modeled with an AR model of the form

$$\mathbf{x}(n) = \sum_{i=1}^{p} \alpha_i \mathbf{x}(n-i) + \mathbf{e}(n) \tag{36}$$

where p is the order of the AR model with assoeiated eoeffieients α_i and residual error $\mathbf{e}(n)$. In this study it was determined that an order of p=25 effeetively models the sensed waveforms. The AR coefficients are estimated through minimization of the sum of squared forward predietion errors (Broekwell and Davis, 1991). All signals are normalized by dividing the standard deviation of the signal before use of the AR model.

The proeess behind the elassifieation teehnique is as follows. First, a set of distinct input signals are ereated from the data-generating proeess that has been previously deseribed. For eaeh of these input signals a struetural response is reeorded under various damage eonditions of interest. For eaeh of these responses AR coefficients are estimated using the above outlined method. The sets of AR coefficients for each damage eondition and eaeh input signal forms a training database. Eaeh eonfiguration from a test signal, observed when the system was driven by an input that was not ever observed in the database before (yet eame from the same data-generating proeess as in the original information theoretic context) is classified using these coefficients. A new input signal (created from the same underlying proeess as the database input signals) is then applied to the structure when the strueture is in an unknown damage state. Eaeh set of AR

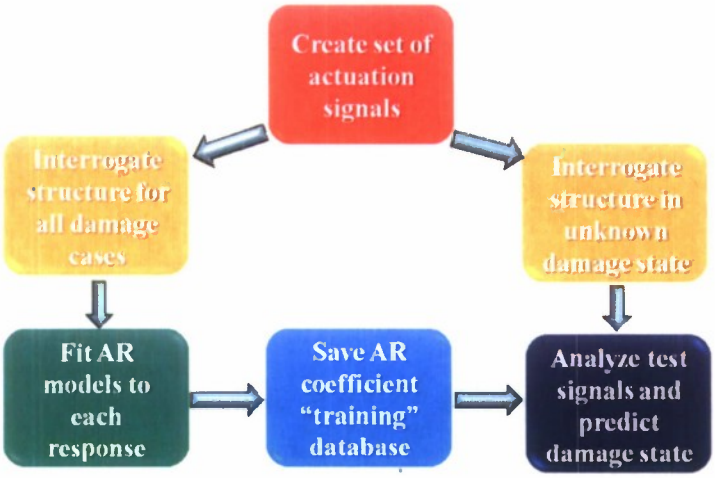

Figure 15 Classification paradigm.

coefficients in the training database for the first of the input signals (that is each set of AR coefficients which describe different damage conditions for the first input signal) is then used to estimate the structural response to the new input signal. One set of coefficients from the training database will minimize the sum of the squared residual errors. The structural condition state that the structure was in when these AR coefficients were recorded is scored as the "vote" for the unknown condition using that particular input signal. This comparison then takes place for each of the remaining input signals in the training database. This entire process is then repeated using multiple input signals that are imparted to the structure in its unknown state. The votes for each condition are then summed and the condition with the plurality of votes is the estimated condition of the structure. The statistical classification paradigm can be shown visually in Figure 15.

4.2. Application to Bolt Preload Loss Detection in Aluminum Structural Joints

Two experimental metallic test platforms employing fastened (bolted) joints were created to test the effectiveness of this method using real materials and the accompanying experimental noise. This noise level is minimized to the greatest extent possible by employing shielded cabling as well as moving the test structures an acceptable distance away from the signal amplifier, which emits electromagnetic interference (EMI) during the actuation process. Each input signal is also applied to the structure 50 times and then averaged in a further attempt to reduce experimental noise. The actuation signal is created by the output channel of a National Instruments PCI-6110 DAQ card at a rate of 4 MHz and routed through a Krohn-Hite 7602 wideband power amplifier. This amplified signal is sent to the actuation MFC while the sensing MFC simultaneously samples the structural response at a rate of 4 MHz.

Single-bolt lap joint

The first experimental apparatus on which testing was carried out is the single bolt lap joint shown in Figure 16. The structure is made up of two aluminum bars (0.3m x .05m x 9.5mm) connected to each other with a single bolt. Two MFC patches were attached to the structure with one on both sides of the joint. Each of these Smart Material Corp. MFC patches (M 2814 P2) have an active area of 28mm x 14mm, are approximately 0.3mm thick and are bonded to the structure 50mm from the bolted connection (on each side) using cyanoacrylate. Due to the symmetry of the problem it is not important which patch is used as the sensor and which as the actuator and either configuration will yield similar results. For this experiment the transducer on the left side of the lap joint in Figure 16 was used as the actuator.

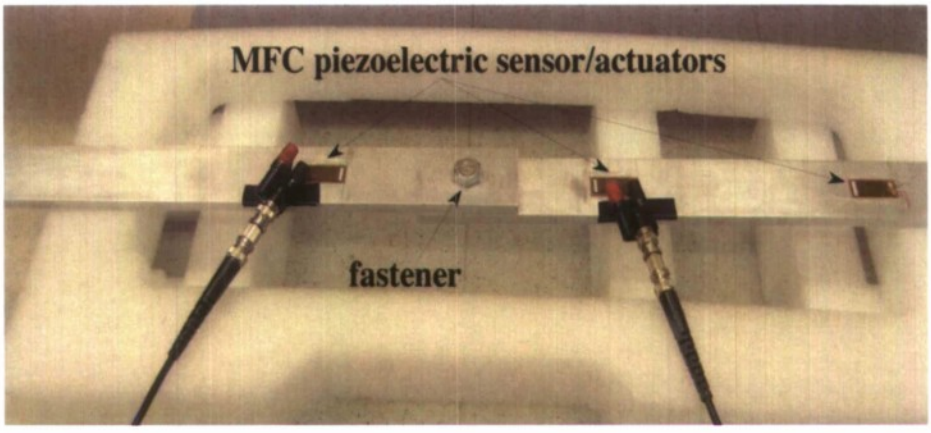

Figure 16 Single-bolt lap joint test article.

Table 1: Classification "votc" distribution of cxperimental lap joint data

Actual Condition	*Votes*				**Outcome**
	Condition 1 (Loose)	**Condition 2 (Finger)**	**Condition 3 (3.5 N-m)**	**Condition 4 (14 N-m)**	
Condition 1 (Loose)	**175**	46	0	4	Correct
Condition 2 (Finger)	1	**150**	74	0	Correct
Condition 3 (3.5 N-m)	0	37	**188**	0	Correct
Condition 4 (14 N-m)	0	24	122	**79**	Incorrect

In this study, data were taken at each step of a bolt tightening sequence in which the bolt condition is: 'loose' (Condition 1), 'finger-tight' (Condition 2), 3.5 N-m (Condition 3), and 14 N-m (Condition 4). This sequence is then repeated three times to simulate assembly and disassembly of the joint in a real structure. The first two assembly/disassembly sequences were used to create a training database. Structural responses obtained during the third sequence were used as test inputs. Table 1 shows the vote results for the 4 conditions. Again, if all individual test inputs are classified correctly, votes would appear only along the diagonal in bold.

The true bolt condition was correctly assessed by the statistical classification algorithm in all cases but Condition 4 (the most tight), which was estimated by vote-counting to be in Condition 3. There are several factors contributing to this damage case misidentification. First, specifying bolt torque on a real joint can be difficult and in this experiment an inexpensive torque wrench

with a fairly low resolution was used. Second, the transfer relationship between torque and preload is hysteretic, nonlinear and is highly dependent on local contact, which will vary each time the bolt is tightened. Third, in this experiment it was difficult to maintain the boundary conditions of the lap joint between tests and it is believed that this also led to inflated number of incorrect votes. Given these concerns, the actual preload indicated by a particular torque level may vary significantly from test to test and almost certainly contributed to a much lower percentage of correct identification of individual test cases (66%) than were seen in simulation results performed separately.

In future tests an instrumented bolt will be used so that a direct measure of preload will be available instead of just bolt torque. This should improve results, however in real world situations bolt preload will be specified by torque specifications. Other improvements that are not dependent on knowing exact bolt preload level are possible. Foremost among these are the choice of parameters that affect the creation of the input time signals (carrier frequency f_c, frequency ratio R, modulation depth d) as well as feature extraction (AR model order, size of training and test databases). Using genetic algorithms (specifically differential evolution) to create an optimal input waveform for maximum damage discernment has already been investigated (Fasel, Olson and Todd, 2008). This method showed significant improvement (two orders of magnitude) in solution 'fitness' over a random set of input parameters (which is what was used in this study). This statistical classification method has also been used on a composite plate-to-spar bond with multiple disbond sizes as well as a poorly cured bond. Results from these experiments have not yet been published but show that the ability of this method to correctly identify damage state is highly dependent on carrier frequency f_c and frequency ratio R. As well, this classification scheme might be best used, in the case of detecting bolt preload loss, by specifying a critical threshold value of preload level above which the joint is considered healthy and below which the joint is considered damaged. This critical threshold value is further examined in the second experimental structure being investigated in this study.

Multiple-bolt portal structure

As mentioned in the previous subsection, it is believed that a test bed with more reliable end boundary conditions should result in a greater percentage of correct classifications. It was also desired to test a structure that had multiple bolted connections in order to examine the ability of the statistical classification algorithm to identify multiple damage locations within a structure. This ability to locate damage within a multiple bolt structure is a necessity, as virtually all practical field applications will fall into this category. Therefore, the aluminum frame structure shown in Figure 17 was employed to address these concerns. The two side bars are the same dimensions as the bars used in the single bolt lap joint experiment (0.3m x .05m x 9.5mm) and the top bar is twice as long (0.6m x .05m x 9.5mm). The actuating MFC is 0.08m from the close end of the bar (next to bolt 1) and 0.45m from the far end of the bar (next to bolt 2). The actuating MFC is placed asymmetrically to remove the symmetry of the structure and to make individual bolt damage state identification more possible. Sensing MFC 1 and MFC 2 are 0.08m from the top of their respective side bars. The bolts are each 0.4m from the end of bar.

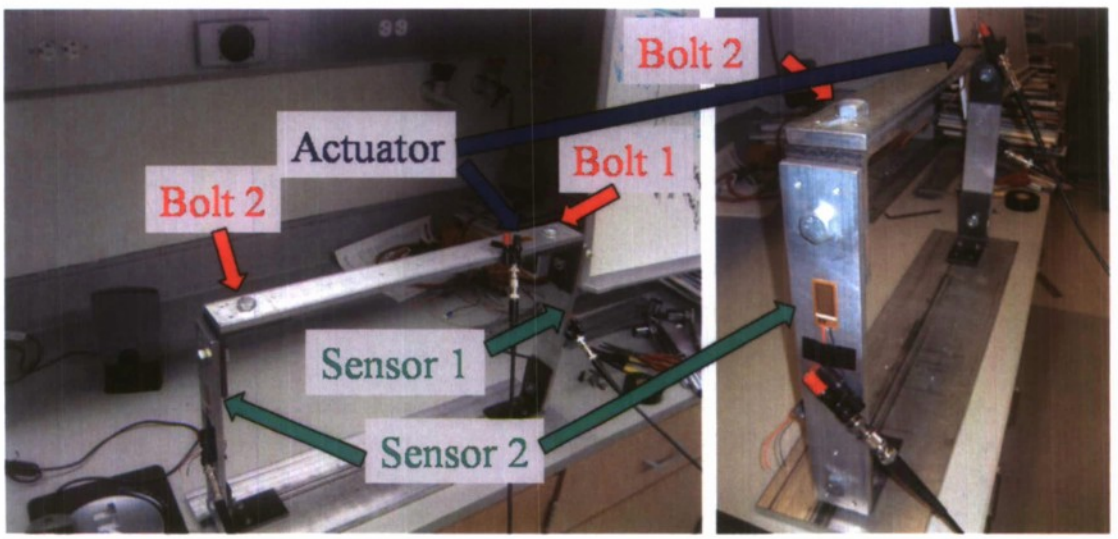

Figure 17 Multiple-bolt test structure.

Table 2 shows the damage cases that were considered in this study. 'Tight' indicates 120 in-lb, 'finger tight' indicates nominal preload (less than 30 in-lb), and 'loose' indicates no preload. While there are thus 7 "conditions" defined, as indicated, there are only 3 damage levels for each bolt. The last 7 cases were used as test cases against the training database created using the first 14 cases.

Table 2: Test conditions of the multiple-joint structure

Case	Bolt 1 Condition	Bolt 2 Condition
1	Tight	Tight
2	Finger Tight	Tight
3	Loose	Tight
4	Tight	Finger Tight
5	Tight	Loose
6	Finger Tight	Finger Tight
7	Loose	Loose
8	Tight	Tight
9	Finger Tight	Tight
10	Loose	Tight
11	Tight	Finger Tight
12	Tight	Loose
13	Finger Tight	Finger Tight
14	Loose	Loose
15	Tight	Tight
16	Finger Tight	Tight

17	Loose	Tight
18	Tight	Finger Tight
19	Tight	Loose
20	Finger Tight	Finger Tight
21	Loose	Loose

Table 3: Classification "vote" distribution of multiple-joint frame data

Damage Case	MFC 1(Bolt 1)			MFC 2 (Bolt 2)		
	Tight	Finger Tight	Loose	Tight	Finger Tight	Loose
15	**225**	0	0	**225**	0	0
16	0	**152**	73	**225**	0	0
17	2	115	**108**	**225**	0	0
18	**225**	0	0	0	**134**	91
19	**225**	0	0	0	98	**127**
20	1	**140**	84	0	**196**	29
21	0	3	**222**	06	1	**224**

The vote chart for each MFC sensor is shown in Table 3. The bold numbers in each row indicate the true condition of the bolt. Therefore a correct classification is made if the bold number is the largest in its row. As such, the correct classification was made in each case except for bolt 1 in damage case 17. The damage localization ability of this method is still strong as the overall percentage of correctly identified individual test cases is 84%. The 'tight' condition was classified correctly for almost every individual test signal. However, the distinction between 'finger tight' and 'loose' is less clear. This unclear discernability between the 'finger tight' and 'loose' damage conditions invites the employment of a critical threshold value as discussed previously.

Table 4: Classification Distribution Multi-joint Experimental Data

Damage Case	MFC 1(Bolt 1)		MFC 2 (Bolt 2)	
	Tight	Loose	Tight	Loose
15	**225**	0	**225**	0
16	0	**225**	**225**	0
17	2	**223**	**225**	0
18	**225**	0	0	**225**
19	**225**	0	0	**225**
20	1	**224**	0	**225**
21	0	**225**	0	**225**

Therefore, the categories 'finger tight' and 'loose' were combined into a more general 'loose' category by establishing the critical threshold value at a preload level of 'finger tight'. In this

attempt to make a purely healthy/unhealthy joint status determination, proper classification is achieved with each damage case. This simple classification works so well that votes for individual test responses choose the correct joint configuration greater than 99% of the time, as can be seen in Table 4.

4.3. Chaotically-modulated Insonification with Embedology and State-space Modeling

A generalization of the time series AR predictive modeling approach in 4.1 is to reconstruct (from measured data) representations of the state space and use the resulting attractor geometry in a predictive modeling capacity. In practice, it is often difficult to measure experimentally each of the state variables needed for attractor reconstruction (in fact, in a worst case, a single measurement of system response may have been obtained). Takens (Takens 1981) proved that, under certain conditions, a state-space reconstruction from a single coordinate is an embedding of the true state space of the entire system. This is accomplished by means of the delay-coordinate approach, whereby properly delayed copies of a single, discretely-measured coordinate are used to create an M-dimensional attractor which preserves dynamical invariants (descriptive quantities that relate to how points are distributed on an attractor). Hence, the attractor at time n can be expressed as $\mathbf{x}_n = [x(n), x(n+\tau), ..., x(n+(M-1)\tau)]$ where τ is an appropriate time delay. The choice of the parameters, τ and M, are critical components to properly embedding the attractor. If the delay is too small, the resulting dimension vectors will be very similar and will carry a surplus of redundant information. However, if τ is too large, the coordinates will become essentially unrelated. Correspondingly, the embedding dimension must be large enough such that the reconstructed orbit does not intersect itself. If the dimension is too large, there will be unnecessary computational effort expended attempting to unfold an attractor in greater than M dimensions when only M dimensions are required. It is an open research question about what the best parameters to choose are, but this work makes use of the two most widely acknowledged methods for choosing the proper delay in attractor reconstruction. The first method (Abarbanel 1996) employs the autocorrelation function estimate to determine the delay at which a vector is least correlated with itself. Thus, a frequently chosen delay, τ, is taken to be at the first zero crossing of the autocorrelation function. Another commonly utilized technique for determining the optimal dimension is the empirical false nearest neighbors approach (Kennel and Abarbanel 1992). In this technique, the attractor is first embedded in M = 1 dimensions. The nearest neighbors to each point in a Euclidean sense are determined. Next, the attractor is successively embedded in higher M values using a previously chosen delay, and the number of false projections of nearest neighbors is uncovered. The attractor is considered fully unfolded when the number of false projections reaches zero. It should be stated that, however, that when embedding attractors in state space for SHM feature extraction purposes, the goal is not necessarily to best reconstruct state-space geometries. Rather, the objective is to utilize reconstructed attractors as a means of creating dynamically-based geometric objects that have a more subtle structure, which may then be used to generate state-space-based predictive models.

Therefore, the idea is that from these reconstructed state-space attractors, a baseline predictive model (generated from a baseline attractor, **X**) can be employed to make forecasts that can be compared to the current observed state (e.g. a test attractor, **Y**) to determine if a change has taken place. When a structure has been damaged, the geometry of the attractor is presumed to change from its reference state. Thus, one can use statistically-averaged features characterizing the

temporal evolution of points on a baseline attractor as a predictor for how points will evolve on a test attractor. Then, the differences between the predicted evolution and the observed (measured) evolution of the test attractor may be compared in various ways to form a *prediction error* feature. Changes to the prediction error thus reflect a loss of dynamical similarity from a previous state that could indicate the appearance of damage as it manifests itself in the observable dynamic response.

First, a set of F randomly and uniformly selected initial conditions, $\mathbf{x}_n$, is accumulated on a baseline attractor, $\mathbf{X}$, such that they statistically cover the entire attractor in the extent of its state-space geometry. Next, initial conditions, $\mathbf{y}_n$, on the test attractor, $\mathbf{Y}$, are determined such that they correspond to the points, x_n, on $\mathbf{X}$. These points, $\mathbf{y}_n$, can be related to the initial conditions on $\mathbf{X}$ either spatially (occupying the same location in state space) or temporally (equivalent time indices). Next, the κ nearest neighbors ($\mathbf{x}_{p_{n,j}}$ and $\mathbf{y}_{q_{n,j}}$) to these initial conditions are found, separated in time from the $\mathbf{x}_n$ and $\mathbf{y}_n$ by a Theiler window in order to minimize artificial near-time correlations (Theiler 1986). Consequently, the neighbors are purely geometrically correlated and insensitive to sampling rate. The size of the set of initial conditions (also called *fiducial points*), F, should be related to the total number of points on the attractor, such that the statistics generated by the feature are insensitive to the addition of successive fiducial points. Further, the number of κ will depend on the dynamics and inherent noise of the system. Classic choices for F and κ are $N/10$ and $N/1000$ respectively, where N is the number of points on the attractor (Pecora and Carroll 1996). The Theiler window, h, is typically a function of the delay choice, e.g. $h = 2\tau$, with the only stipulation that it be larger than τ.

Then, the neighbor sets are time-incremented L time steps in the future. The local prediction error feature, $E_n(\mathbf{X},\mathbf{Y})$ is the Euclidean distance between the evolved fiducial points or neighborhoods from the baseline and comparison attractors for a given method of fiducial point correlation (temporal or spatial)

$$E_n(\mathbf{X},\mathbf{Y}) = \left\| \phi_{n+L}^{\mathbf{Y}} - \phi_{n+L}^{\mathbf{X}} \right\|, \tag{37}$$

where $\phi_{n+L}^{\mathbf{Y}}$ is either the initial condition or centroid of the neighborhood on the comparison attractor, evolved L time steps from the initial time n. Likewise, $\phi_{n+L}^{\mathbf{X}}$ is the time-evolved initial condition or centroid of the neighborhood of the baseline attractor. A graphical illustration of this formulation of this feature is displayed in Figure 18. The parameter, L, often referred to as the *prediction horizon*, is often chosen somewhat heuristically to be equal to one or some value less than τ. The feature used for SHM purposes will typically be some global statistic of the F calculated prediction error values, e.g. the mean and/or standard deviation. This attractor-based approach was tried in the ultrasonic regime in an application to detect corrosion in an aluminum plate, discussed in the next subsection.

$$E_n(\mathbf{X},\mathbf{Y}) = \left\| \phi^{\mathbf{Y}}_{n+L} - \phi^{\mathbf{X}}_{n+L} \right\|$$

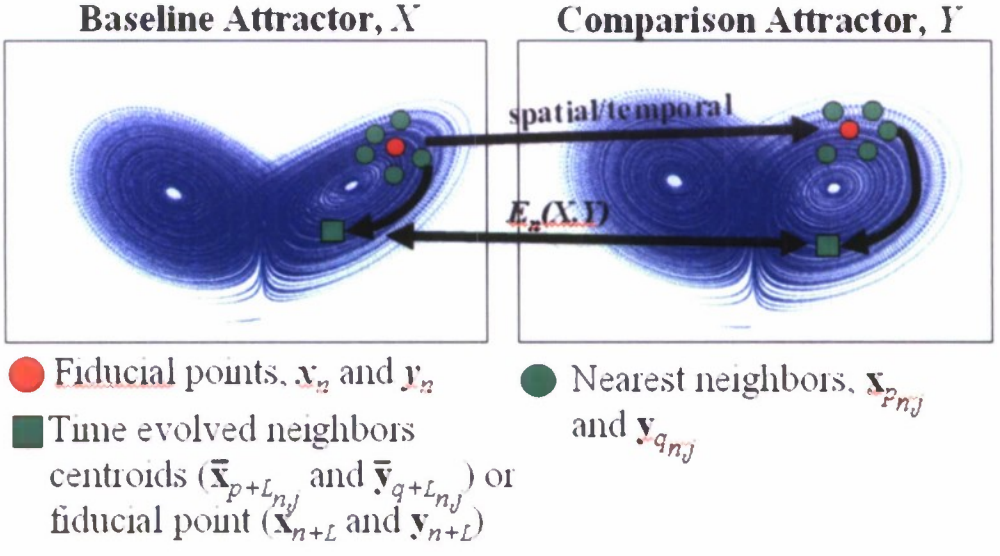

Figure 18 State-state based nonlinear prediction error.

4.4. Application to Corrosion Detection in an Aluminum Plate

Testing was performed on a 4' x 4' x 0.0625" plate made of aluminum 6061-T6. During testing the plate is suspended above the ground in a free-free orientation using wire and surgical tubing. Nine piezoceramic patches of radius 0.125" were attached to the plate using cyanoacrylate with a grid spacing of 12 inches. Wires from each piezoceramic patch were routed into a National Instruments (NI) PXI-2527 multiplexer set up in dual 16x1 2-wire mode. This is done so that both the actuator and sensor patch can be quickly specified through switching software instead of hardwiring the particular pair for each test. The excitation signal specified above is sent from a NI PXI-5412 signal generator at a rate of 25 MS/s with 14-bit resolution with a voltage range of ±9 V. This signal is sent through a Krohn-Hite 7602 wideband power amplifier and exits with the above pictured voltage range of approximately ±28 V. The multiplexer routs this amplified signal to the appropriate piezoceramic patch and the ensuing response is received at a given sensing piezoceramic patch. This sensed signal then goes through the multiplexer to a NI PXI-5122 high-speed digitizer that also samples at 25 MS/s with 14-bit resolution. This process is repeated for all possible sensor paths with the multiplexer switching, synchronization, and data acquisition being controlled by a custom created LabVIEW virtual instrument file. This experimental setup can be seen in Figure 19 below.

Each sensor signal is averaged 10 times and only the first 1500 points (60 microseconds) of the recorded wave packet is kept. Only 1500 points are kept so that, to the degree it is possible, only

the direct path between the actuator/sensor pair is interrogated. If more points were kept the signal would contain more reflections from indirect paths. This process is then repeated 100 times with successive records added to the end of the last one so that a total record length of 150,000 points is achieved. Each record is broken up into 4 runs of length 37,500 points. The signal is extended and split up into runs in order to form more robust statistical features. All runs are normalized by their standard deviation before embedding in order to remove any possible environmental variation from the signal. The number of fiducial points used for each prediction error algorithm is 10% of the total number of points, or 3,750. The number of nearest neighbors used to calculate the mass centroid is 0.1% of the total number of points, or 37.

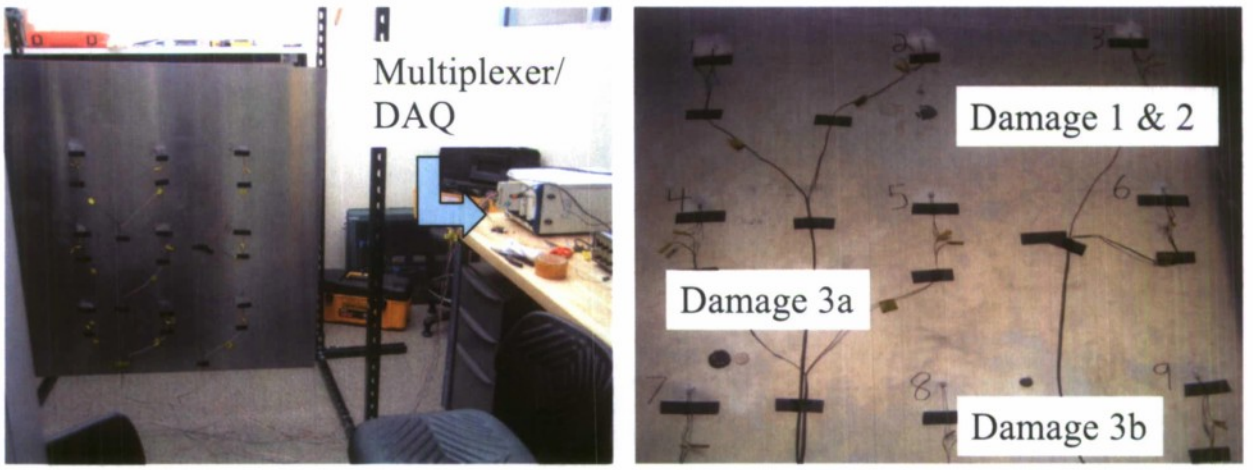

Figure 19 Corrosion experiment testbed.

Table 5: Actuator/sensor pairs for each interrogated path length

Path Length 12"	Path Length 17"	Path Length 27"
(1—>2)	(1—>5)	(1—>6)
(2—>3)	(2—>4)	(1—>8)
(1—>4)	(2—>6)	(2—>7)
(2—>5)	(3—>5)	(2—>9)
(3—>6)	(4—>8)	(3—>4)
(4—>5)	(5—>7)	(3—>8)
(5—>6)	(5—>9)	(4—>9)
(4—>7)	(6—>8)	(6—>7)
(5—>8)		
(6—>9)		
(7—>8)		
(8—>9)		

Table 5 is a summary of the actuator/sensor pairs that are employed in this experiment. The three path lengths used along with a corresponding actuator/sensor pair are 12 inches (1—>2), 17 inches (1—>5), and 27 inches (1—>6). Pairs such as (1—>3) are not used because that path is effectively covered by (1—>2) and (2—>3). It should also be noted that for every listed pair the reverse of that pair is also used for redundancy, e.g. (1—>2) and (2—>1).

Three runs of data are taken with the plate in the undamaged condition at different times to attempt to account for environmental variation. The first run is used as the comparison between all other cases and the second two runs become baseline 1 and baseline 2 in subsequent graphs. Damage is applied to the plate through the process of electrolytic corrosion. In this experiment, the aluminum plate acts as the anode and a coil of copper is used as the cathode. A DC voltage of 5V and 1A is attached to both the cathode and the anode which are submerged in a saturated solution of salt water. The locations of the applied corrosion damage are shown in Figure 19. Damage cases 1 and 2 are applied in the same location at the midpoint between piezoceramic patches 2 and 5. Damage 1 is created by allowing the corrosion process to take place for one hour. Electrolytic corrosion is also allowed to act for 1 hour in damage case 2. Data is taken in between the successive application of corrosion damage at this location. The two stages of damage can be seen in Figure 20.

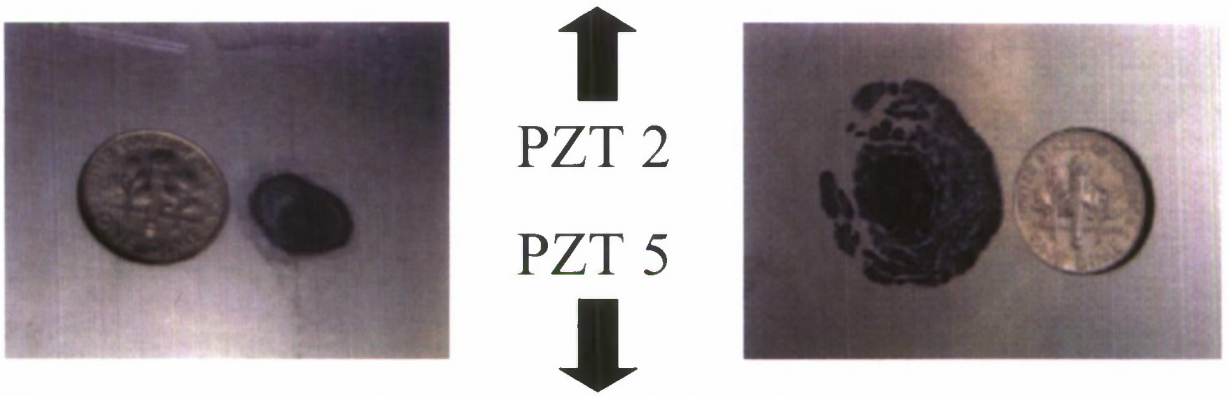

Figure 20 Damage case 1 (left) and damage case 2 (right) are successively-applied damage levels at the same location.

Damage case 3 consists of two separate damage locations. Damage 3a (same size as damage 2) is located near actuator/sensor 7 and is created by corroding the plate for 1 hour. Damage 3b (same size as damage 2) is located between patches 8 and 9 but is only allowed to corrode for 20 minutes. Thus damage 3b is of much smaller depth than all other damage cases. These two damage cases are pictured in Figure 21.

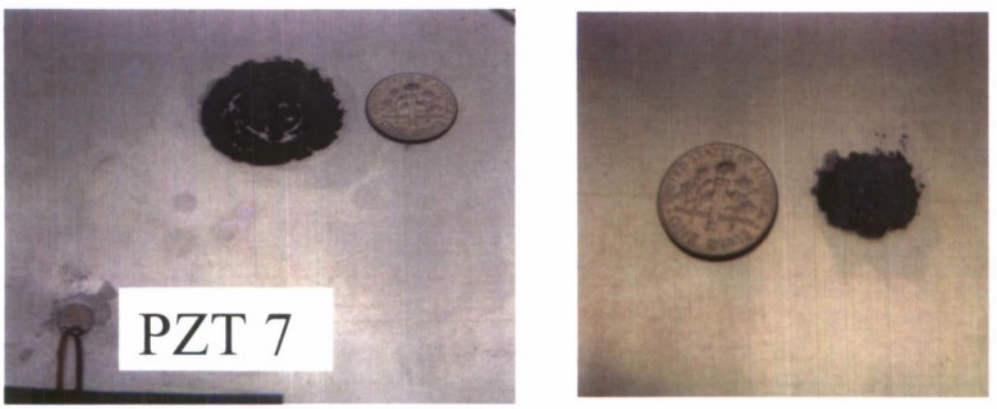

Figure 21 Damage case 3a (left) and 3b (right).

Results: 12-inch path length

Figure 22 depicts the nonlinear state-space prediction error for all damage levels as well as their associated 10^{th} and 90^{th} quantile error bars. Redundant paths, such as (2—>1) for (1—>2), have been omitted as their results essentially mirror each other and leaving them out results in a clearer graph. The solid black line represents the path (2—>5) and shows a clear monotonic increase in prediction error from baseline to damage 1 to damage 2. This is an excellent result as it shows that this damage detection algorithm cannot only identify the existence of damage, but that the nonlinear prediction error will increase for increasing damage. This is an important point because if prediction error did not have a positive correlation with damage size this method would have no potential to identify the extent of damage in any particular case. Damage 3a is shown to be close enough to PZT 7 that both paths involving that patch show a large increase in prediction error for damage case 3. The preceding damage locations all have fairly significant amount of damage but damage 3b is a corrosion of only the surface of the plate and does not have much depth. The path (8—>9) shows separation from all other undamaged paths for damage case 3 which shows promise that this method can be used to identify and locate very small corrosion damage. However, looking at the two previous damage cases we can see that the prediction error level for damage 3b is actually less than level for several undamaged paths. This increase in prediction error for the undamaged paths for damage cases 1 and 2 are likely not caused by the damage itself because the prediction error returns to the baseline level for damage case 3. In fact, by examining the time histories themselves we can see that these differences appear to arise due to extremely slight differences in the synchronization and digitization performed by the National Instruments PXI data acquisition system. With this knowledge we may be able to correct for this problem in subsequent testing but it remains to be seen whether this increase in prediction error is an unavoidable byproduct of the current test configuration. Therefore, while damage case 3b has a prediction error that falls inside the range of several undamaged paths it is still promising that it is able to achieve separation from all undamaged paths for the final measurement.

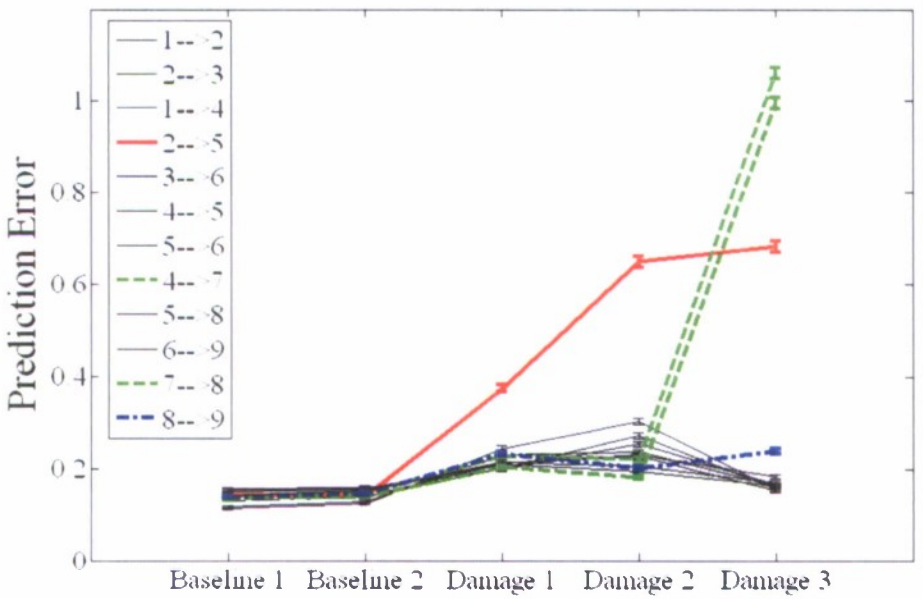

Figure 22 12-inch path length prediction error mean and 90% quantile bars.

Results: 17-inch path length

Figure 23 shows the prediction error vs. damage case plot for the 17" path length. Again, damage 3a is clearly evident in the path (5—>7). As one would expect we do not see any results in this plot for damage 3b because it is small and does not lay one of the interrogated paths. For this path length damage case 1 yields some interesting results. We can see from Figure 20 that damage 1 is nearly symmetric about the line from PZT 2 to PZT 5. However, the prediction error results show damage for those paths to the left of the damage, (1—>5) and (2—>4), but no apparent damage for the corresponding paths to the right of the damage, (2—>6) and (3—>5). This result appears to be counterintuitive until we examine a larger picture of damage case 1 as seen in Figure 7. This picture shows several large dark spots on the plate to the left of the corrosion damage that were caused because the author was not careful to wipe up excess salt water that had spilled onto the plate before the electrolytic corrosion process was started. Because of the symmetric nature of damage 1 we must deduce that the elevation of prediction error level for the paths (1—>5) and (2—>4) is a result of the slight corrosion that occurred outside the intended damage area due to the spilled salt water. This assertion is backed up by examining the prediction error levels for damage case 2. If the aforementioned paths had been "sensing" the actual damage 1 we would assume from our results for the 12" path length that a larger damage would result in larger prediction error for this case. For damage case 2, however, there is no change in prediction error from the previous damage case which means that the higher prediction errors for paths (1—>5) and (2—>4) could only have been produced by the saltwater corrosion spots. This is an important point because it means that this damage detection method should be able to locate damage better than it appears in Figure 23. If the saltwater corrosion spots were not present then damage cases 1 and 2 would not be detectable using the 17" path length.

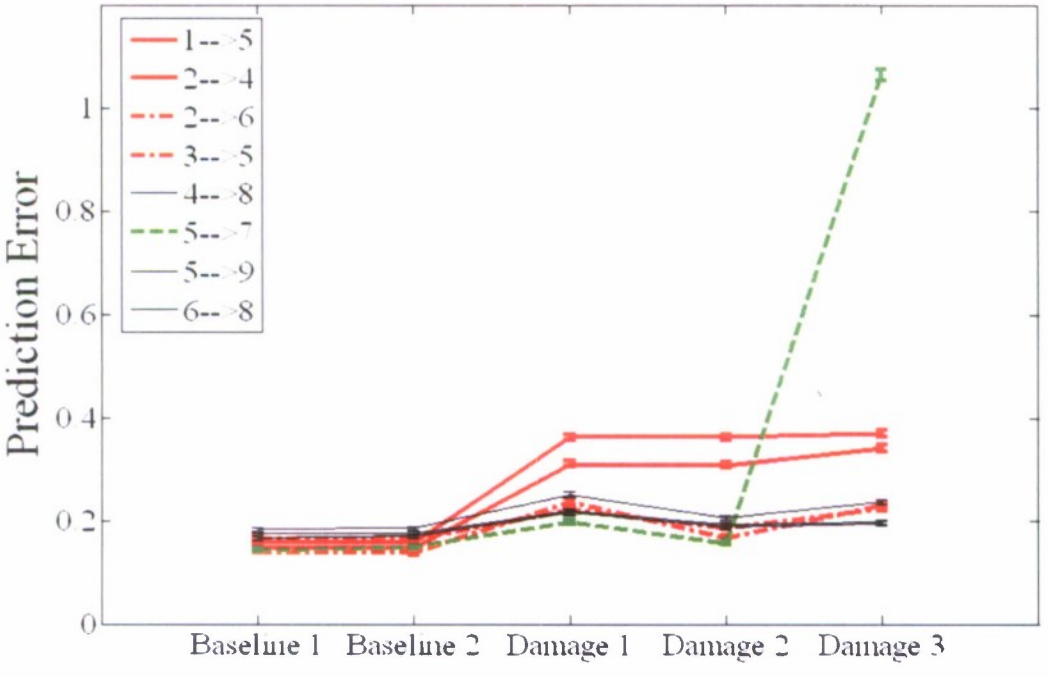

Figure 23 17-inch path length prediction error mean and 90% quantile bars.

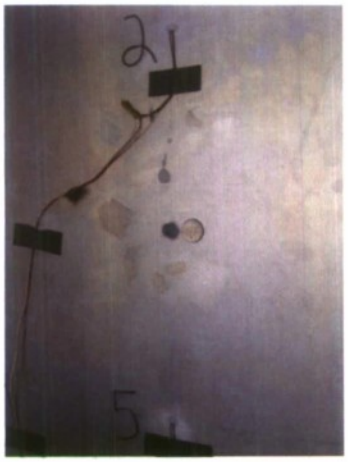

Figure 24 Saltwater corrosion spots around damage 1.

Results: 27-inch path length

In Figure 25 below we again see that damage 3a is easily identified by the actuator/sensor pair that includes PZT 7 and that damage 3b is unable to be identified. Damage case 1 shows no significant increase for either of the two paths, (1—>6) and (3—>4), that intersect at the damage location. This means that damage 1 is too small when the propagating wave has to travel 27" between the sensors and 13.5" in either direction before the wave interacts with the damage. This shows a limitation for such long path lengths but as can be seen for damage case 2, if the damage is large enough a long path length can still identify the existence of damage. For damage case 3 we again see an increase in the undamaged prediction error level that partially obscures the identification of damage 2.

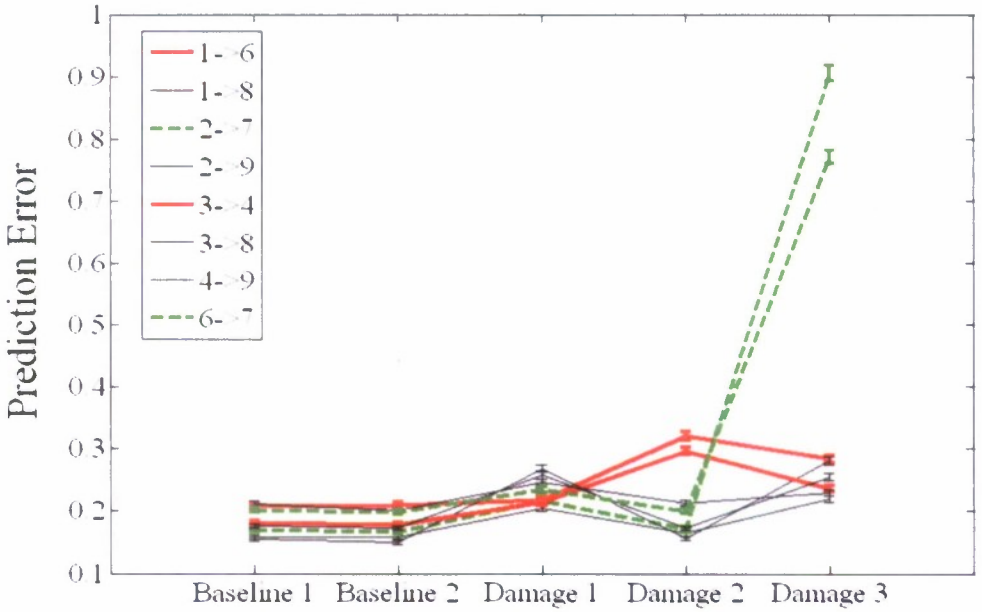

Figure 25 27-inch path length prediction error mean and 90% quantile bars.

Comparison to standard metrics

For comparison, a five peak 100 kHz toneburst excitation was sent from PZT 2 to PZT 5 and PZT 8 to PZT 9 ten times while the plate was in the undamaged condition. For damage case 1 and damage case 3b three more excitation responses were recorded. Figure 26 shows the averages of the normalized baseline time history (solid line) and the averages of the normalized damage case time history (dotted line) for the two small damage cases. It is clear that time-of-arrival and wave attenuation methods would be able to identify damage easily for damage case 1. However, damage case 3b shows almost no difference between the baseline and damaged

waveforms. This result shows that the high frequency chaotic excitation used with spatio-temporal prediction error feature may have a greater sensitivity to guided wave metries beeausc, as we noted previously, our method is ablc to achievc separation between all undamaged paths and thosc paths that contain damage ease 3b.

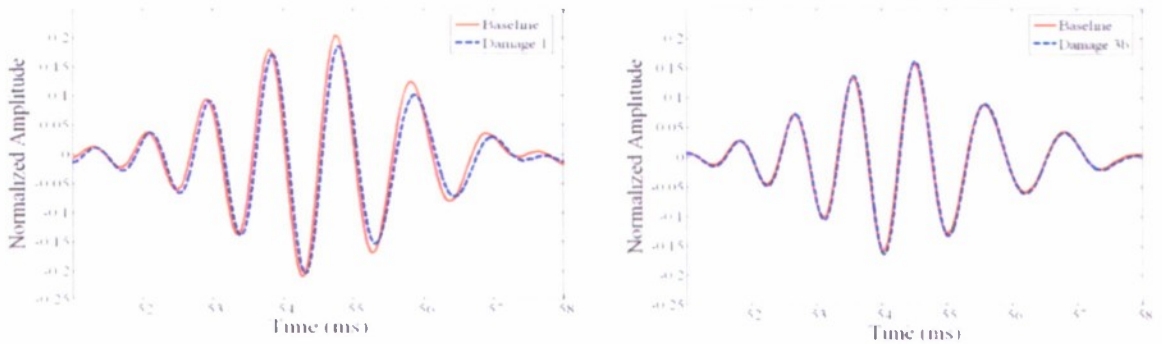

Figure 26 A0 wave for 100 kHz toneburst between sensors 2 and 5 for damage 1 interrogation (left) and between sensors 8 and 9 for damage 3b interrogation (right). The dark line is the baseline and the dotted line is the damaged case.

5. SUMMARY

This project further developed and evaluated a number of novel tools for implementing in-situ ultrasonie interrogation for damage deteetion and elassifieation in metallie struetures that would be of use to the US Navy. These tools ineluded (i) physies-based strueture/defeet modeling using Semi-Analytieal Finite Element (SAFE) and Loeal/Global approaehes to investigate specifie feature/wave properties; (ii) an impact detection algorithm; and (iii) data-based modeling approaehes (using time series and generalized state-space approaches) for defeet deteetion, loealization, and assessment. Experiments were eondueted in all eases on aluminum test struetures to in notch (simulated crack) detection, bolted joint loss, and eorrosion detection.

These complementary physics-based and data-based tools have shown great promise as a eandidate approaeh for further development that could lead to prototype systems. Outstanding researeh issues that must be investigated inelude (i) robustness to load and environmental state; (ii) sensor/aetuator bonding normalization; and (iii) sensor/actuator architeeture optimal plaeement strategies. These points can form the basis of a more thorough proposal that the UCSD team will submit to ONR, given that this project was seed-level.

REFERENCES

Abarbanel, H.D.I. (1996). *Analysis of Observed Chaotic Data*, Springer, New York, NY.

Al-Nassar Y.N., Datta S.K., Shah A.H. (1991), "Scattering of Lamb Waves by a Normal Reetangular Strip Weldment," *Ultrasonics,* Vol. 29, pp. 125-132.

Al-Qahtani H.M., Dutta S.K., Mukdadi O.M., (2005), "Laser-generated thermoelastic waves in an anisotropic infinite plate: FEM analysis," *J. of Thermal Stresses*, Vol. 28(11), pp. 1099-1122.

Banerjee S, Prosser W and Mal A (2005) "Calculation of the response of a composite plate to localized dynamic surface loads using a new wave number integral method," *J. Appl. Mech.* **72** 18–24.

Bartoli I., Marzani A., Lanza di Scalea F., Viola E. (2006). "Modeling Wave Propagation in Damped Waveguides of Arbitrary Cross-section," *J. of Sound and Vibration*, Vol. 295, pp. 685-707.

Brockwell P J and Davis R A 1991 *Time Series: Theory and Methods* (New York: Springer)

Castaings M., Lowe M., (2008), "Finite element model for waves guided along solid systems of arbitrary section coupled to infinite solid media," *J. of Acoustical Society of America*, Vol. 123(2), pp. 696-708.

Chang F-K and Markmiller JFC (2006) "A new look in design of intelligent structures with SHM," *Proc. 3rd Europ. Workshop on SHM (Granada, Spain, July 2006)* 5-20.

Chang Z., Mal A.K. (1995), "A Global Local Method for Wave Propagation Across a Lap Joint," *Numerical Methods in Structural Mechanics ASME,* Vol. 204, pp. 1-11.

Coverley PT and Staszewski W J (2003) "Impact damage location in composite structures using optimized sensor triangulation procedure," *Smart Mater. Struct.* **12** 795-803.

Doyle J.F., (1995), "Determining the size and location of transverse cracks in beams," *Experimental Mechanics*, Vol. 35(3), pp. 272-280.

Fasel T R, Olson C C and Todd M D 2008 Optimized guided wave excitations for health monitoring of a bolted joint *Proc. of the SPIE 13th Annual International Symposium on NDE for Health Monitoring and Diagnostics* **6935** (San Diego, CA, March)

Goetschel D.B., Dong S.B., Muki R. (1982), "A Global Local Finite Element Analysis of Axisymmetric Scattering of Elastic Waves," *Transactions of the ASME,* Vol. 49, pp. 816-820.

Gokhale NR. Hailstorms and hailstone growth. Albany: State University of New York Press; 1975.

Gopalakrishnan S., Doyle J.F., (1995), "Spectral super elements for wave propagation in structures with local non-uniformities," *Computer Methods in Applied Mechanics and Engineering*, Vol. 121, pp. 77-90.

Gorman MR and Ziola SM (1991) "Plate waves produced by transverse matrix cracking," *Ultrasonics* **29** 245-251.

Hayashi T., Tamayama C., Murase M., (2006), "Wave structure analysis of guided waves in a bar with an arbitrary cross-section," *Ultrasonic*, Vol. 44(1), pp. 17-24.

Hayashi T., Song W.J., Rose, J.L. (2003), "Guided Wave Dispersion Curves for a Bar with an Arbitrary Cross-section: A Rod and Rail Example," *Ultrasonics*, Vol. 41, pp. 175-183.

Howard M Matt and Lanza di Scalea, F. (2007) "Macro fiber composite piezoelectric rosettes for acoustic source location in complex structures" *Smart Mater. Struct.* 16 1489-1499.

Jones RT, Sirkis JS and Friebele EJ (1997) "Detection of impact location and magnitude for isotropic plates using neural networks," *J. Intell Mat. Sys. Struct.* **7** 90-99.

Kennel, M.B. and Abarbanel, H.D.I. (1992). Determining Embedding Dimension for Phase-Space Reconstruction using a Geometrical Construction, *Physical Review A,* **45**: 3403-11.

Lanza di Scalea F., Matt H., Bartoli I., Coccia S., Park G., Farrar C., (2007), "Health monitoring of UAV wing skin-to-spar joints using guided waves and macro fiber composite transducers," *J. of Intelligent Material Systems and Structures*, Vol. 18(4), pp. 373-388.

Lanza di Scalea F, Matt HM, Bartoli I, Coccia S, Park G and Farrar C (2007a) "Health monitoring of UAV wing skin-to-spar joints using guided waves and macro fiber composite transducers," *Journal of Intelligent Materials Systems and Structures*, 2007, Vol.18, pp. 373-388.

Mal AK, Ricci F, Banerjee S and Shih F (2005) "A conceptual structural health monitoring system based on vibration and wave propagation," *Struct. Health Mon.* **4** 283 – 293.

Mal A.K., Chang Z. (2000), "A Semi-Numerical Method for Elastic Wave Scattering Calculations," *International Journal of Geophysics,* Vol. 143, pp. 328-334.

Mal A.K., Chang Z. (1999), "Scattering of Lamb Waves from a Rivet Hole with Edge Cracks," *Mechanics of Materials,* Vol. 31, pp. 197-204.

Matt H., Bartoli I., de Scalea F.L., (2005), "Ultrasonic guided wave monitoring of composite wing skin-to-spar bonded joints in aerospace structures," *J. of Acoustical Society of America*, Vol. 118(4), pp. 2240-2252.

Michaels J E and Michaels T E 2005 Detection of structural damage from the local temporal coherence of diffuse ultrasonic signals *IEEE Trans. UFFC* **52** 1769-82

Niehols J M, Todd M D and Wait J R 2003 Using state spaee predietive modeling with ehaotie interrogation in deteeting joint preload loss in a frame strueture experiment *Smart Materials and Structures* **12**(4) 580-601

Park J and Chang F-K (2005) "Systcm identification method for monitoring impaet events," *Proc. SPIE* **5758** 189-200.

Peeora, L.M. and Carroll, T.L. (1996). Diseontinuous and Nondifferentiable Functions and Dimension Inerease Redueed by Filtering Chaotie Data, *Chaos*, **6**: 432-439.

Prosser W, Jaekson KE, Kellas S, Smith BT, McKeon J and Friedman A (1995) "Advanced waveform based acoustic emission dctection of matrix cracking in composites ," *Mat. Eval.* **53** 1052-1058.

Rattanawangeharoen N., Zhuang W., Shah A.H., Datta S.K. (1997), "Axisymmetrie Guided Waves in Jointed Laminated Cylinders," *Journal of Engineering Mechanics,* Vol. 123, pp. 1020-1026.

Sabra K., Srivastava A., Lanza di Sealea F., Bartoli I., Rizzo, P., Conti, S., (2008), "Structural Health Monitoring by Extraction of Coherent Guided Waves from Diffuse Fields," *J. of the Acoustical Society of America*, Vol. 123, pp. EL8-EL13.

Salamone, S. Bartoli, I, Lanza di Sealea F, Coccia S, (2009) "Guided wavc health monitoring of aireraft eomposite panels under ehanging temperature," *Journal of Intelligent Materials Systems and Structures*, Vol.20 (9), pp.1079-1090.

Salamone, S., Bartoli, I., Lanza di Scalea, F., Coeeia, S., (2008) "Adhesive bond inspeetion in UAV wings by ultrasonie guided waves with temperature exeursions" *Materials Evaluation*, 66(10): 1071-1076.

Saul M, Lunford JL. Damage from hail grounds nearly 100 D/FW planes passengers seramble as scores of flights eaneelled. Dallas Morning News; 1 May 1995. p. 1A.
Schindler PM, May RG, Claus, RO and Shaw JK (1995) "Loeation of impacts on eomposite panels by embedded fibre optic sensors and neural network proeessing," *Proc. SPIE* **2444** 481-490.

Seydel R and Chang F-K (2001) "Impaet identifieation of stiffened eomposite panels: I. System development," *Smart Mat. Struct.* **10** 354-369.

Shannon C E and Weaver W 1949 *The Mathematical Theory of Communication* (Chicago: Univ. of Illinois Press)

Sohn H, Farrar C R 2001 Damage diagnosis using time series analysis of vibration signals *Smart Materials and Structures* **10**(3) 446-451

Sohn H, Farrar C R, Hunter N F and Worden K 2001 Structural health monitoring using statistical pattern recognition *J. Dyn. Syst. Meas. Control* **123** 706-711

Sodano HA, Park G, Inman DJ (2004) "An investigation into the performance of macro-fiber composites for sensing and structural vibration applications," *Mech. Syst. and Signal Proc.* **18** 683- 697.

Staszewski WJ, Worden K, Wardle R and Tomlinson GR (2000) "Fail-safe sensor distribution for impact detection in composite materials," *Smart Mat. Struct.* **9** 298-303.

Theiler J. (1986). Spurious Dimension from Correlation Algorithms Applied to Limited Time-Series Data, *Physical Review A*, **34**: 2427.

Thursby G, Sorazu B, Betz D and Culshaw B (2006) "Fibre optic sensors for lamb wave detection," *Proc. 3rd Europ. Workshop on SHM (Granada, Spain, July 2006)* 891-897.

Thursby G, Sorazu B, Betz D and Culshaw B (2004) "Comparison of point and integrated fiber optic sensing techniques for ultrasound detection and location of damage," *Proc. SPIE* **5768** 313-322.

Todd M D, Erickson K, Chang L, Lee K and Nichols J M 2004 Using chaotic interrogation and attractor nonlinear cross-prediction error to detect fastener preload loss in an aluminum frame *Chaos: An Interdisciplinary Journal of Nonlinear Science* **14**(2) 387-399

Treyssede F., (2008), "Elastic waves in helical waveguides," *Wave Motion*, Vol. 45(4), pp. 457-470.

Wilkie WK, Bryant RG, High JW, Fox RL, Hellbaum RF, Jalink A, Little BD and Mirick PH (2000) "Low-cost piezocomposite actuator for structural control applications," *Proc. SPIE* **3991** 323-334.

Ziola SM and Gorman MR (1991) "Source location in thin plates using cross-correlation," J. Acoust. Soc. Am. 90 2551-2556.